Confocal Microscope for quantum computing using NV Center in diamonds

A Thesis

submitted to

Indian Institute of Science Education and Research Pune
in partial fulfillment of the requirements for the
Master of Science in Quantum Technology

by

Deepanshu

Indian Institute of Science Education and Research Pune

April, 2026

Supervisor: Prof. Umakant D. Rapol

Certificate

This is to certify that this dissertation entitled "Confocal Microscope for quantum computing using NV Center in diamonds " submitted towards the partial fulfilment of the Master of Science in Quantum Technology represents study/work carried out by Deepanshu from Indian Institute of Science Education and Research Pune under the supervision of Dr Prof. Umakant D. Rapol (Indian Institute of Science Education and Research Pune) during the academic year 2025–2026.

Signature of Supervisor (Prof. Umakant D. Rapol) Date: 18 May 2026

Signature of Advisory Member (Prof. T. S. Mahesh) Date: _____

Declaration

I hereby declare that the matter embodied in the report entitled "Confocal Microscope for quantum computing using NV Center in diamonds " are the results of the work carried out by me at the Indian Institute of Science Education and Research Pune under the supervision of Prof. Umakant D. Rapol (Indian Institute of Science Education and Research Pune) and the same has not been submitted elsewhere for any other degree.

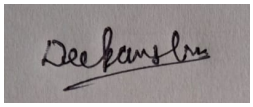

Signature of the Author (Deepanshu) Date: 13-05-2026

Abstract

Nitrogen-Vacancy (NV) centers in diamond have been identified as a highly promising system for implementing quantum technology owing to its extended spin coherence duration, operation at room temperature operations, and optical control and readout. In this work, a confocal microscope is constructed and used for exploring both optical and spin features of the NV centers that are useful for quantum computing.

With confocal microscope, spatially resolved measurements on single NV centers become possible while also providing a way to efficiently collect photons emitted by them. With this approach, optically detected magnetic resonance (ODMR) experiments are carried out to study the NV center spin-related fluorescence response. Resonance dips arising from the transitions between ground state spins are successfully measured and thus the value of zero field splitting and other perturbing factors are precisely determined.

With a fully developed confocal microscope, in the future, many experiments can be designed, such as a multi-qubit gate and entanglement between nuclear and electronic spins. And to work with specially engineered diamonds.

Acknowledgements

I would like to express immense gratitude to my supervisor, Prof. Umakant D. Rapol, for giving me an opportunity to work in his lab, the Atomic Physics and Quantum Optics Lab, where I explored lot of new techniques as an experimental physicist. His constant guidance,support, and encouragement always motivated me to learn more and to push my limits.

I would always be thankful to Dr. Shouvik Datta with whom my journey to explore experimental physics started. Also allowing the use of the Vector Network Analyser (VNA) for the characterisation of microwave antennas whenever needed.

A special thanks to Dipansh Rajput, Trivijay Jawale and Kshitija Satao. Dipansh started the work on NV centres before I joined the lab, and his experience and insights were helpful in performing various experiments. Trivijay Jawale for his constant support in the development of the ARTIQ control system whenever required. Kshitija Satao made the Pizeo x-y stage, which was needed for scanning the diamond sample.

I sincerely thank I-Hub IISER Pune, CEO iHUb Dr Kunj Tandon, and Niranjan Deshmukh for granting us access to their facilities and resources.

To my lab mates, Rayees AS, Joel M., Sunil, Monu Bhartiya, Shuvarti Roy, and the rest of the group, for always guiding me with the experimental techniques needed for developing the experimental setup.

Finally, I thank my parents who always believed in and supported me; without their support, I would never have come to this place.

Contents

List of Figures

List of Tables

Chapter 1

Introduction

Quantum computers are considered the future of the next generation of high-speed computational systems. They use the laws of quantum mechanics to perform computing, quantum phenomena like superposition, entanglement and quantum interference form the backbone of the quantum computing [8]. The difference between Quantum and classical computers is that in quantum computers, information is stored and processed through the usage of qubits, which is a two-level quantum system capable of quantum superposition and exhibiting entanglement.

With further development in technology, quantum computing will revolutionize various areas such as cryptography, materials science, simulation, optimization, and machine learning [9, 10]. At present there are problems that need to be overcome like decoherence and error correction, but at the same time, progress continues and makes quantum computing one of the core technologies for the future.

Various platforms are being explored to bring quantum computers into use, some them are ion trap, neutral atom and solid state systems [11, 12]. In this thesis solid state system are being explored, Nitrogen-Vacancy(NV) center in diamonds, which is a promising candidate because of various reasons like operation at room temperature, long spin coherence time, optical readout and coherent manipulation of spins using microwave fields [3, 13]. These properties make NV center a suitable candidate for various other fields as well like quantum communication, quantum sensing and metrology.

1.1 NV Centers as Qubits

In NV centers, the electronic ground state is a spin triplet i.e. $S = 1$, with spin sublevels $m_s = 0, \pm 1$. The spin levels $m_s = 0$ and $m_s = \pm 1$ in the absence of external magnetic field, are separated by zero field splitting of approximately $D_{gs} = 2.87\ GHz$ and spin state $m_s = \pm 1$ shows degeneracy. These spin sublevels forms a suitable

two-level system for encoding quantum information and computing [14].

The major advantage of the NV centers is their spin-dependent fluorescence. When they are optically pumped with a green laser(532nm) they get polarized into $m_s = 0$ state, then microwave field can be used to manipulate spin and because of spin-dependent fluorescence they can be optically readout. These three features of spin initialization, spin manipulation and optical readout, forms the basis for NV center to be used as qubits.

These three processes combined also form the basis for optically detected magnetic resonance (ODMR), where recording the change in fluorescence as a function of microwave frequency is monitored [15]. This ODMR form the basis of the high-sensitivity quantum sensing application, such as magnetic field, temperature and strain.

1.2 Role of confocal Microscopy

Harnessing single NV Centers in diamond lattice requires a highly efficient optical addressing and spatial resolution system. A crucial role is played by confocal microscopy by enabling diffraction-limited imaging, which helps in mapping, detecting and selectively exciting single NV centers.

Confocal microscopy is based on the use of a tightly focused laser beam to excite small region within the sample and in the path of detection a pinhole is placed, to reject out-of-focus fluorescence, and collecting only the signal originating from the focal plane. As a consequence, confocal microscopy can contribute in studying isolated single NV centers in the bulk diamond.

The integration of confocal microscope with control system, such as microwave excitation and photon detection system, allows for performing optical and spin measurement simultaneously. The combined setup of confocal microscope and control system allows to perform various experiment such as ODMR, spin rabi oscillation and various quantum control operation [4].

1.3 Objective of this thesis

The objective of this thesis is to design a confocal microscope with full control system, that can be used to perform various quantum experiments on NV centers. The specific goals include:

- To design a confocal microscope for high-resolution imaging of NV centers.
- To integrate various control and measurement systems such as SINARA, Swabians Time tagger, to develop a fully controllable system to perform various experiments.

- To design and implement various pulse sequences to perform experiments like raster scan, CW-ODMR, PW-ODMR and Differential ODMR.

1.4 Thesis outline

The organization of this thesis is given below:

Chapter 2 talks about the theoretical background of the NV centers, starting from the synthesis of NV center, their electronic and optical properties, what makes NV centers a good candidate for Quantum application and how quantum gates can be implemented.

Chapter 3 talks about the implementation of experimental set up of the confocal microscope, how control system in integrated with it. And various pulse sequence to perform experiments.

Chapter 4 discuss the various results obtained, including confocal scan, CW-ODMR, PW-ODMR, and Differential ODMR.

Chapter 5 discuss the conclusion and future outlook of the work done.

Chapter 2

Background / Literature Review

2.1 Diamonds

One of the allotropes of carbon is diamond, which is one of the hardest naturally occurring materials found on Earth. They have applications in many fields, starting from gemstones for jewellery, to industry use for cutting and polishing hard materials, in the medical field for blood vessel stents, microprobes, and artificial joint components [16] because of their various mechanical, optical and thermal properties.

Over the past few decades, they have been explored as one of the promising candidates for Quantum sensing, Quantum information and computing, because of the presence of the colour center defects, like negatively charged Nitrogen-Vacancy (NV^-) center with unique properties such as coherence time ranging from microseconds to seconds, operation at room temperature, and the capability for optical initialization and readout, on which we will be focusing in this thesis.

2.1.1 Characteristics of Diamonds

Natural diamonds are composed of two isotopes of carbon, namely C-12 and C-13, with their natural concentrations of 98.9% and 1.1%, respectively, with C-12 having I = 0 nuclear spin and C-13 having a nuclear spin of I = $\frac{1}{2}$. Their lattice structure is Face Centered Cubic (FCC), in which each carbon atom is sp^3 hybridized and forms a covalent bond with four other carbon atoms in a tetrahedral arrangement. They have a high energy bandgap of 5.47eV between valence and conduction bands, which corresponds to a wavelength in the ultraviolet range, making them transparent to visible light. At room temperature, the thermal conductivity of diamond is 2200 W/mK, which is the highest among all materials, which makes it an excellent heat conductor [17]. See Fig. 2.1 for a schematic of the tetrahedral bonding configuration of carbon atoms in diamond.

In natural diamonds, impurities and defects result in colour centres that give

natural diamond its different colors. Nitrogen is one of the most common impurity found in diamond that replaces carbon in diamond's crystal lattice and forms NV centers. NV centers in diamond can be in three charge states NV^-, NV^+ and NV^0, but NV^- centers have received much attention due to their potential quantum application.

Apart from this, in recent decades, much progress has been made in the synthesis of diamonds, as discussed in the next section, using techniques such as HPHT and CVD, through which good quality synthetic diamonds with desirable properties, including NV centers, can be synthesized.

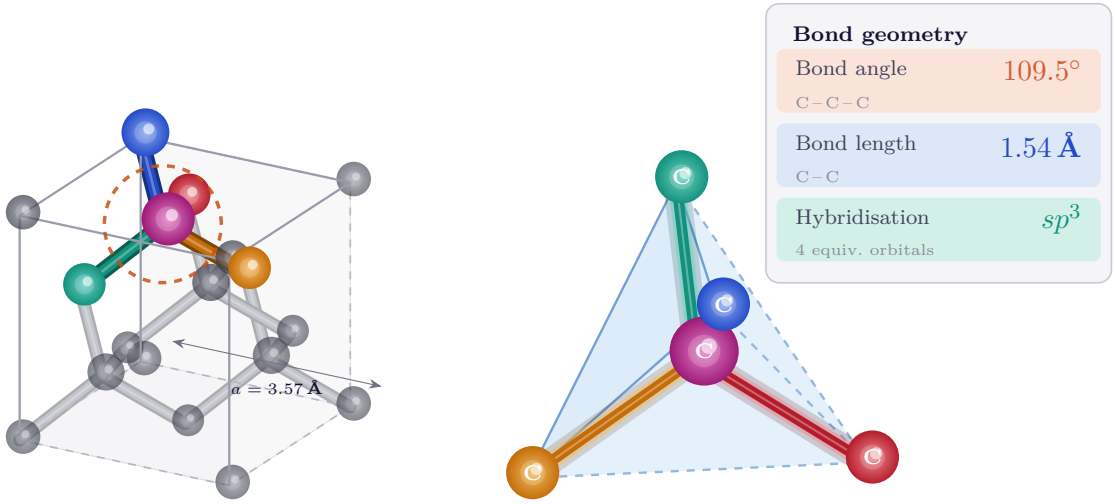

(a) Diamond Cubic (FCC) Unit Cell **(b)** sp^3 Tetrahedral Bonding Site

Figure 2.1: Diamond crystal structure. **(a)** The face-centred cubic (FCC) unit cell of diamond with lattice parameter $a = 3.57$ Å. One complete tetrahedral bonding unit is highlighted in colour: the central basis atom (magenta) bonds covalently to one corner neighbour C_1 (blue) and three face-centre neighbours C_2–C_4 (teal, amber, crimson). **(b)** Enlarged sp^3 tetrahedral bonding site. The bond angle (109.5°) is marked between the amber and crimson bonds. The bond-geometry panel summarises the C–C bond angle, bond length $d = 1.54$ Å, and sp^3 hybridisation. Atom colours correspond directly to those in (a).

2.1.2 Synthesis of Diamonds

With recent advancements in technology, controlled synthesis of diamonds has been made possible, which has made the production of high quality research grade diamonds with desirable properties, such as controlling the concentration of C-12 and C-13 isotopes, concentration of nitrogen impurities, and the creation of NV centers. Two primary methods used for the synthesis of diamonds are High Pressure High Temperature (HPHT) and Chemical Vapour Deposition (CVD).

High Pressure High Temperature (HPHT) Method

As the name suggests, in this method, a carbon sample is placed under high pressure in the range of 5-10 GPa and high temperature of about 2000°C conditions to form di-

amond; mostly graphite is used as the carbon source [2, 18]. Under this condition, the phase transition from graphite to diamond can take place, where the metal catalyst: iron, nickel, or cobalt, which helps to lower the energy barrier for the transformation. This method is best to create highly doped diamonds with a high concentration of nitrogen impurities.

Chemical Vapor Deposition(CVD)

In this method, conditions for pressure and temperature are much lower than the HPHT method, pressure is in the range of 20-30 mbar and temperature is about 800°C [4]. In this process, carbon gas such as methane (CH_4) is introduced into a vacuum chamber along with hydrogen gas (H_2) where diamond surface is used as seed layer for the growth of diamond. On this layer, plasma of hydrogen is created which helps to break the methane gas into carbon and hydrogen atoms and under ambient conditions, pure diamond grow layer by layer.

With this method, the isotopic concentration of carbon can be controlled, by using isotopically enriched methane gas, a diamond crystal with high purity can be formed, with specific properties, such as long coherence times for quantum applications.

The CVD method also allows for the inclusion of nitrogen impurities during the growth process, which is essential for creating NV centers in diamond. And in this high purity diamond, the implantation of nitrogen ions can be done to create NV centers with high precision and control over their spatial distribution

Classification of Diamonds

Diamonds can be classified according to the impurities and defects in their crystal lattice, which give rise to different types of diamonds with distinct properties. The most common classification is based on the concentration and distribution of nitrogen , as shown in Table 2.1.

Type	N Content	Sub-type	Description	[N] (ppm)
I	High	Ia	Nitrogen atoms present as aggregates within the lattice	< 3000
		Ib	Isolated substitutional nitrogen atoms	< 500
II	Low	IIa	Extremely low nitrogen impurity concentration	~ 1
		IIb	Presence of boron impurities; exhibits p-type conductivity	< 1

Table 2.1: Classification of natural diamonds based on nitrogen content and distribution [5].

2.2 The NV-Centers

The Nitrogen vacancy (NV) centers are atomic-scale defects in the diamond lattice. It consists of a nitrogen atom substituting a carbon atom, located next to a lattice vacancy These defects act as trapped atom-like quantum systems in a solid-state host. They have discrete electronic energy levels and optically addressable spin states [3, 13]. The NV center has C_{3v} symmetry and can be oriented along one of the four crystallographic $\langle 111 \rangle$ directions in the diamond lattice.

They are naturally found in diamonds because of the natural occurrence of nitrogen impurities in diamonds. With time, lattice vacancies are trapped near the nitrogen impurities, thus forming nitrogen vacancy centers. In chemical vapour deposition (CVD) and high-pressure high-temperature (HPHT) diamonds, nitrogen vacancy centers are typically created during the growth process. In ultra-high purity diamonds, the density of nitrogen vacancy centers is very low, with as few as a single nitrogen vacancy center in a volume of $10^4\,\mu\text{m}^3$.

For diamonds with high nitrogen concentration, it has been found that the density of nitrogen vacancy centers can be greatly increased by introducing additional lattice vacancies. This has been achieved by high-energy electron irradiation, which produces a uniform vacancy distribution within several micrometre depths. Annealing at temperatures above 600°C, the vacancy becomes mobile, while the nitrogen atoms are fixed in the lattice. Consequently, lattice vacancies will diffuse throughout the lattice and combine with nitrogen atoms at substitutional lattice sites, thus forming nitrogen vacancy centers.

Alternatively, ion implantation techniques allow for the formation of vacancies. The ion implantation of nitrogen ions into diamonds with low levels of intrinsic nitrogen has been performed [19, 20]. Both the nitrogen and the vacancies can be introduced in this way. The subsequent annealing process helps in the formation of

the NV centers. Additionally, the vacancies introduced in this process can pair with the existing levels of impurity in the diamonds, thus creating the NV centers.

However, the efficiency of creation of the NV centers in this process is strongly dependent on the implantation energy. As the ion implantation energy is reduced from MeV range to the keV range, the number of created vacancies decreases. This leads to the lesser formation of NV centers. Additionally, the implantation depth decreases with the reduction in the ion implantation energy. The vacancies created in this process tend to be close to the surface. They tend to recombine in this region. Subsequent implantation of additional vacancies by carbon ions helps in overcoming this problem.

2.2.1 NV center's Electronic Structure

NV centers exist in two optically active charge states: NV^0 and NV^- state [21]. These charge states are distinguished from their zero phonon lines(ZPLs) in the emission spectra, as shown in figure 2.2 [1]. The NV^- state is of particular interest due to its unique electronic and spin properties.

The NV^- state has six electrons in its electronic configuration, three electrons are from the dangling bonds of the neighbouring carbon atoms surrounding the vacancy, nitrogen has five valence electrons out of which three make a covalent bond with the first nearest carbon atoms, the remaining two electrons are localized within the vacancy site. And the sixth electron is captured from an external donor, thus making it negatively charged.

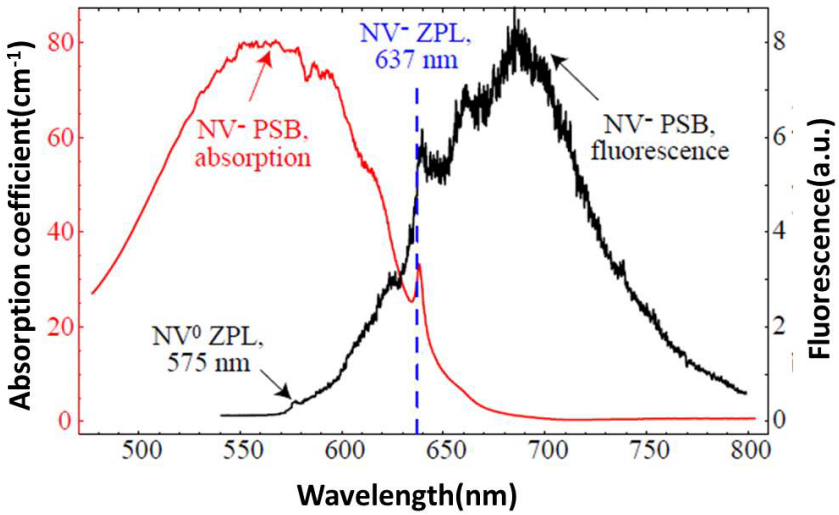

Figure 2.2: Photoluminescence spectra of NV^0 and NV^- centers. The NV^0 center exhibits a zero phonon line (ZPL) at 575 nm, and the NV^- center has a ZPL at 637 nm.. This figure is taken from [1].

The electron density in NV^- state is highly localised at the vacancy site and nearest neighbour carbon atoms, because of which its electronic state can be represented by molecular orbital theory [2]. According to the linear combination of atomic orbitals(LCAO), a set of four orbitals is formed. They exist between the diamond band gap and can be described as a linear combination of sp^3 orbitals of the nitrogen atom and three carbon atoms. Based on group theoretical models, the electronic structure of the ground and excited states is defined by the distribution of six electrons across the lower-lying a_1 orbitals and the energetically degenerate e_x and e_y molecular orbitals. The a_1 orbitals are non-degenerate and lie lower in energy, while the e_x and e_y are degenerate and lie higher in energy, as shown in fig 2.3 [2].

NV centers have spin triplet ground state ($^3A_2$) with total spin quantum number $S = 1$.

In this configuration, two electrons are in lower-energy a_1 orbitals, while the remaining four electrons are distributed into the higher-energy e_x and e_y orbitals.

Similarly, a spin triplet state excited state (^3E), where one electron is promoted from the a_1 orbital to the e_x or e_y orbital, resulting in a different electronic configuration.

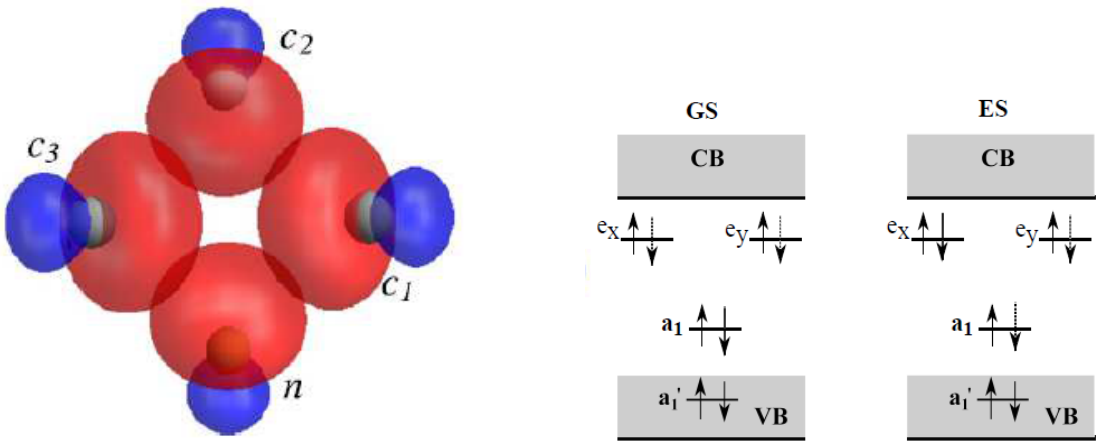

Figure 2.3: Group theoretical analysis of the NV center: (a) Molecular orbital model of NV^- with $c_1, c_2, c3$ as carbon atom and nitrogen(n) surrounding the vacancy (b) spatial orbital distribution. [2]

2.2.2 Optical Properties and Inter system Crossing

As discussed earlier, the NV^-centre has a spin triplet ground state ($^3A_2$) and an excited state (^3E), with spin sublevels corresponding to $m_s = 0$ and $m_s = \pm 1$. When no external magnetic field is present , the spin sublevels of both the ground and excited

states show a splitting of D_{gs}=2.87 GHz and D_{es}=1.42 GHz respectively, because of the spin-spin-dipole interaction of the unpaired electrons [4]. Apart from this, there are metastable singlet states ($^1A_1$ and ^1E) that lies between the ground and excited states, as shown in fig 2.4, which makes NV centers a special system.

The transition between these states is optically allowed, having a zero phonon line (ZPL) at 637 nm. When the NV center is optically excited with off-resonant frequency such as 532 nm, the population is pumped to the phonon sideband of the excited state. During this excitation process, the spin state is preserved, i.e $\Delta m = 0$. However, when the system decays back to the ground state; it can take two pathways :

1. **Radiative Decay:** This path is followed when system is in $m_s = 0$ state and decays by direct transition from excited state to ground state, this is a spin conserving path and while decaying to ground state it emits fluorescence in the wavelength range of 637-800nm.

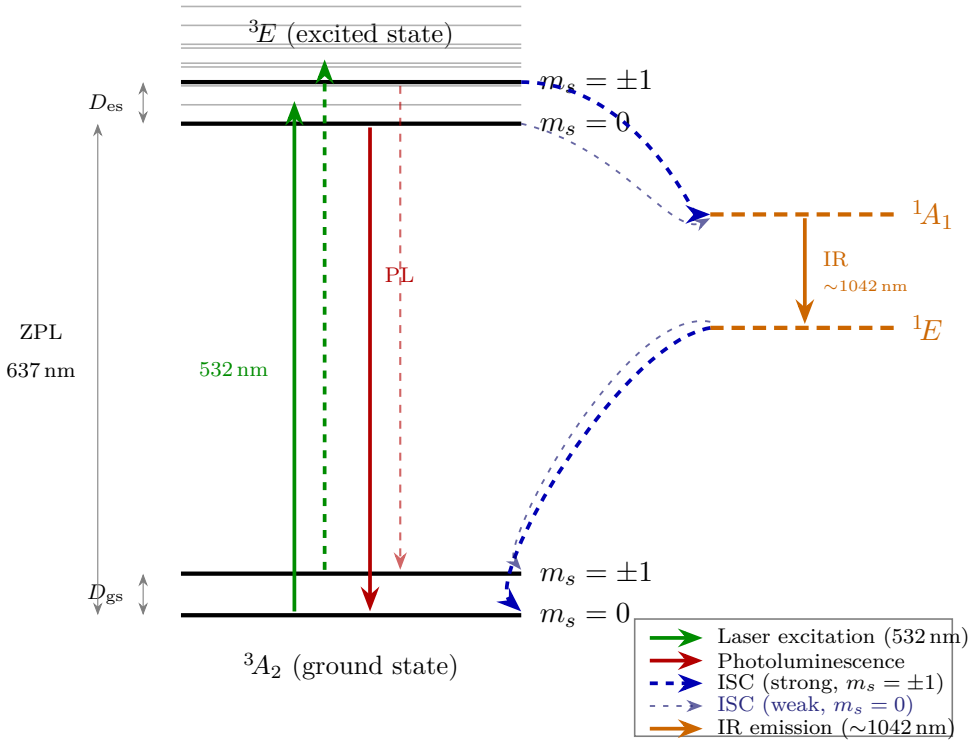

Figure 2.4: Energy level diagram of the NV$^-$ center, illustrating the ground state ($^3A_2$), excited state (^3E), and intermediate singlet states ($^1A_1$ and ^1E). The diagram shows the optical excitation (green arrows), photoluminescence (red arrows), intersystem crossing (ISC) pathways (blue arrows), and infrared emission (orange arrow). The ISC pathways are differentiated by their strength, with solid lines indicating strong ISC for $m_s = \pm 1$ and dashed lines indicating weak ISC for $m_s = 0$. This figure is adapted from [3].

2. **Non-Radiative Intersystem Crossing (ISC):** An alternative decay route where the population in the ^3E state from the $m_s = \pm 1$ sublevels, crosses into

the metastable singlet states ($^1A_1$ and ^1E). From these singlets, the system predominantly relaxes into the $m_s = 0$ sublevel of the ground state without emitting any fluorescence. And this process is not spin conserving, which leads to the spin polarization into the $m_s = 0$ sublevel of the ground state. This is a crucial mechanism that enables optical initialization and readout.

2.3 Spin Hamiltonian

The electronic ground state hamiltonian of the NV^- center depends on the spin-spin interaction, Zeeman effect, and hyperfine interaction. The hamiltonian is divided into following:

$$H = H_{\mathrm{ZF}} + H_{\mathrm{EZ}} + H_{\mathrm{HF}} + other\ terms \tag{2.1}$$

where H_{ZF} is the zero-field splitting term, H_{EZ} is the electronic Zeeman term, H_{HF} is the hyperfine interaction term,

2.3.1 Zero-Field Splitting

As discussed earlier, the zero-field splitting originates from the spin-spin interaction between the two unpaired electrons in the e_x and e_y orbitals in the ground state. It is expressed as

$$H_{\mathrm{ZF}} = DS_z^2 + E(S_x^2 - S_y^2) \tag{2.2}$$

where $D = 2.87\ GHz$ represents the axial zero-field splitting parameter, E is the transverse zero-field splitting parameter [21]. The axial term D causes a splitting of the $m_s = 0$ and $m_s = \pm 1$ sublevels, while the transverse term E can lead to mixing of the $|m_s = \pm 1\rangle$ states, especially under any strain or electric fields.

2.3.2 Zeeman Interaction

Zeeman splitting happens when the electronic spin interacts with the external magnetic field $\mathbf{B}$, which leads to the splitting of $m_s = \pm 1$. This interaction is described as :

$$H_{\mathrm{EZ}} = g_e \mu_B \, \mathbf{B} \cdot \mathbf{S} = \mathrm{h}\gamma_e(\mathbf{B} \cdot \mathbf{S}) \tag{2.3}$$

where μ_b is the bohr magneton, $\mathrm{g}_e(2.0023)$ is electron g-factor and γ_e is the electron gyromagnetic ratio. If the external magnetic field is aligned along the NV quantization axis, then the hamiltonian is given as :

$$H_{\mathrm{EZ}} = \mathrm{h}\gamma_e(\mathbf{B}_z\mathbf{S}_z) \tag{2.4}$$

which result in linear splitting of the degenerate state as a function of applied magnetic field and resonance frequencies for transitions from $m_s = 0$ to $m_s = \pm 1$ is giving as :

$$\nu_{\pm} = D + \pm\gamma_e B_z \tag{2.5}$$

Magnetic field Measurement

The difference between these two resonance frequencies can provide the magnitude of the magnetic field along the NV axis:

$$\Delta\nu = \nu_+ - \nu_- = 2\gamma_e B_z \tag{2.6}$$

This forms the basis for the NV center based Magnetometer.

2.3.3 Hyperfine interaction

The interaction of the electronic spin with the surrounding nuclear spin gives rise to this HF splitting of spin sublevels. Apart from the C^{12} which has zero nuclear spin quantum number ($I = 0$), NV surrounding can have C^{13} with nuclear spin quantum no as $I = \frac{1}{2}$, N^{14} with nuclear spin quantum number as $I = 1$ and N^{15} with nuclear spin quantum number as $I = \frac{1}{2}$. This leads to the additional splitting of the m_s spin levels into total of $\mathrm{m}_I = 2I+1$ sublevels as shown in fig 2.5

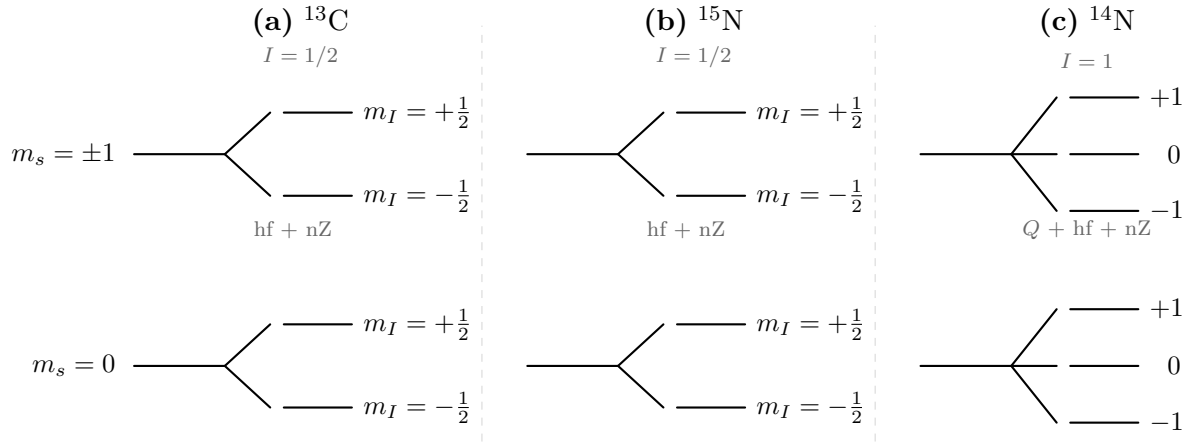

Figure 2.5: Hyperfine structure of the NV^- center for different nuclear spins: (a) ^{13}C ($I = 1/2$), (b) ^{15}N ($I = 1/2$), and (c) ^{14}N ($I = 1$). The splitting arises from hyperfine (hf), nuclear Zeeman (nZ), and quadrupole (Q) interactions. Reproduced from [4]

The hyperfine interaction consists of isotropic Fermi contact interaction H_F and anisotropic electron-nuclear magnetic dipole-dipole interaction H_{dd} [4] defined as:

$$\hat{H}_{hf} = \hat{H}_F + \hat{H}_{dd} \tag{2.7}$$

$$\hat{H}_F = \frac{2\mu_0}{3}\,\gamma_e g_n \mu_n\,|\psi^e_{en}|^2\,\hat{\mathbf{S}}\cdot\hat{\mathbf{I}} = a_{\text{iso}}\,\hat{\mathbf{S}}\cdot\hat{\mathbf{I}} \tag{2.8}$$

$$\hat{H}_{dd} = \frac{\mu_0}{4\pi}\,\gamma_e g_n \mu_n\,\frac{\hat{\mathbf{S}}\cdot\hat{\mathbf{I}} - 3(\hat{\mathbf{S}}\cdot\mathbf{e}_r)(\mathbf{e}_r\cdot\hat{\mathbf{I}})}{r^3} \tag{2.9}$$

where

- μ_0 is the permeability of free space.
- γ_e and g_n are the electron gyromagnetic ratio and nuclear g-factor, respectively.
- μ_n represents the nuclear magneton.
- $|\psi^e_{en}|^2$ is the electron spin density at the nucleus.
- a_{iso} is the isotropic hyperfine coupling constant.
- r is the separation distance between the electron and nuclear spins, with $\mathbf{e}_r$ being the corresponding unit vector.

Since the Fermi contact interaction depends on the electron spin density near the nucleus, which means the nuclear spins very close to the NV center are of interest. Whereas the dipole-dipole interaction is a long-range interaction and decays very fast as it is directly proportional to $\frac{1}{r^3}$. This can be summarized as:

$$H_{\text{HF}} = \mathbf{S}\cdot\mathbf{A}\cdot\mathbf{I} \tag{2.10}$$

where $\mathbf{A}$ is the hyperfine tensor refer table 2.2 for more details and I is the nuclear spin. Refer table 2.2 for more details

Nuclear spin	**Spin** (I)	**Hyperfine splitting (MHz)**	γ (kHz/G)
^{13}C (multiple lattice sites)	1/2	0 to 126	0.3077
^{14}N	1	-2.16	-0.4316
^{15}N	1/2	$+3.03$	1.071

Table 2.2: Hyperfine interaction strengths for NV^- centers. The splitting of ESR lines arises from the contact hyperfine interaction with nearby nuclear spins. The gyromagnetic ratio γ is also listed. The values are taken from [5, 7].

2.4 Optically Detected Magnetic Resonance

As discussed in Section 2.2.2, the NV center exhibits spin-dependent fluorescence, which combined with the zeeman splitting makes the basis for the Optically Detected Magnetic Resonance.

ODMR is a technique which is used for the measurement of the magnetic field, finding resonance frequencies for the transitions $m_S = 0$ to $m_s = \pm 1$.

In ODMR experiment at some external magnetic field, the spin sublevel is polarised to $m_s = 0$ by the application of a green laser(532nm), which is also called as spin initialization. A microwave field is employed to drive transitions between spin sublevels of the ground state. When microwave frequency is swept, and the corresponding fluorescence is recorded, then at resonance frequency transitions between $m_S = 0$ to $m_s = \pm 1$, a change in fluorescence takes place as shown in fig 2.6. This happens because of the ISC, and the splitting between the degenerate states is because of zeeman effect, which can also be seen in the ODMR spectrum. From this splitting, we can extract the information about the applied magnetic field and the resonance frequency. Detailed explanation about experimental protocols for ODMR is given in section 3.3

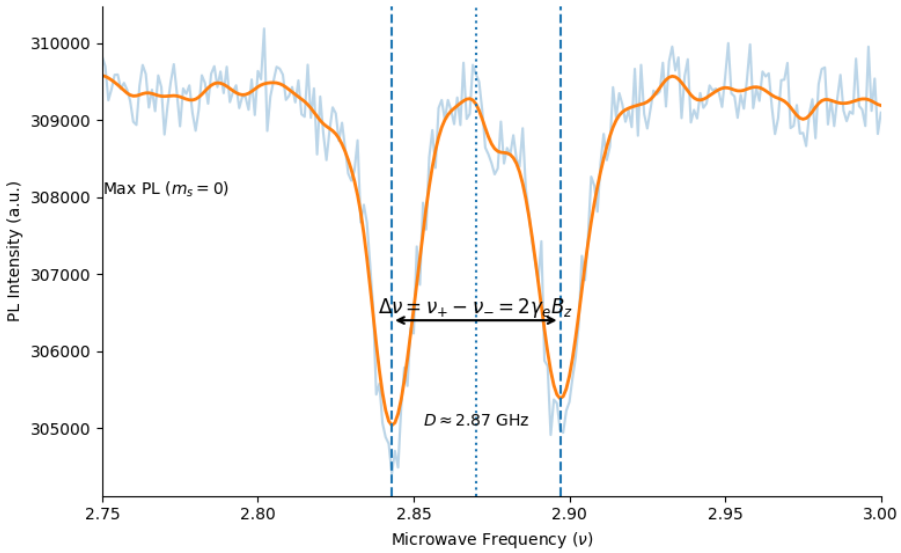

Figure 2.6: ODMR spectrum of an NV center showing fluorescence dips corresponding to the transitions $m_s = 0 \rightarrow m_s = \pm 1$. The splitting of the dips arises due to the Zeeman effect in the presence of an external magnetic field. This data was taken on the confocal microscope built in the lab at some magnetic field.

2.5 Spin Rabi oscillations

Since NV centers can be treated as a two-level quantum system by the spin sublevels $m_s = 0$ and $m_s = \pm 1$ of the ground state, so rabi oscillations can be observed in this system when it is driven by resonant microwave field. From Rabi oscillations, we can extract the information about the exact time period of microwave pulse required to fully transfer the spin state from $m_s = 0$ to $m_s = \pm 1$ which is known as π pulse.

To observe the Rabi oscillation, a pulse sequence as shown in fig **??** can be designed. The system is first prepared in $m_s = 0$ state by a pulse of green laser (532nm), Then, a pulse of microwave frequency, with a varying time duration, is applied, and the resulting fluorescence intensity is measured. Since $m_s = 0$ is a bright state and $m_s = \pm 1$ is a dark state, it will be observed that the signal is showing an oscillating behaviour. The probability of finding the system in state $m_s = 0$ is given as:

$$P_{m_s=0}(\tau) = \frac{1}{2}\left[1 + \cos(\Omega_R \tau)\right], \tag{2.11}$$

where Ω_R is the Rabi frequency, which depends on the strength of the applied microwave field and τ is the microwave pulse duration.

Ideally rabi oscillations should not decay over time, but due to the interaction of the spin with the nearby spin bath, it starts to decay. This decaying is related to the decoherence processes which lead the spin to loss it's phase coherence with the spin state. These decaying oscillations can be defined as :

$$P_{m_s=0}(\tau) = \frac{1}{2}\left[1 + e^{-\tau/T_2^*}\cos(\Omega_R \tau)\right], \tag{2.12}$$

where T_2^* is the dephasing time of the system.

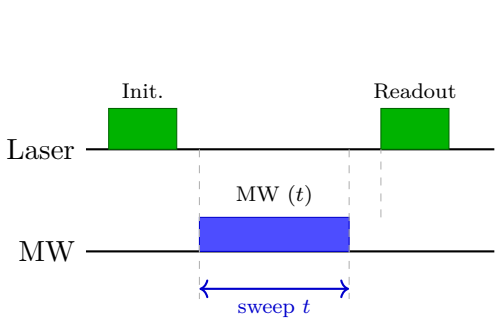

(a) Rabi pulse sequence.

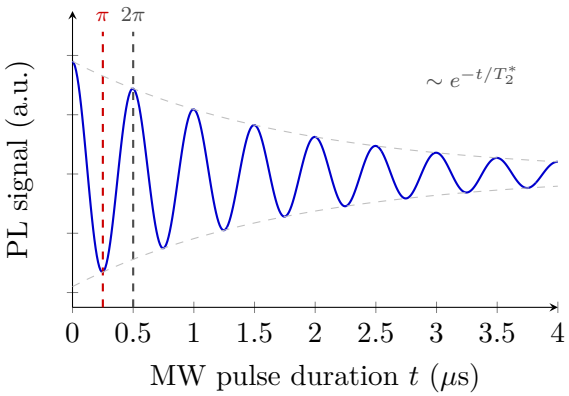

(b) Decaying Rabi oscillation.

Figure 2.7: Electronic spin Rabi oscillation of an NV centre. (a) Pulse sequence: laser initialization, variable MW pulse of duration t, laser readout. (b) Photoluminescence vs. MW duration showing Rabi oscillations decaying with T_2^*. Dashed lines mark the π and 2π pulse durations [5].

So, by measuring the Rabi oscillations, we can get information about the coherence properties of the system, duration of π and $\frac{\pi}{2}$ pulses with which we can manipulate the spin state and form the basis for quantum control, quantum gates and quantum computing. Some other methods like the Ramsey Interferometer can also be used to observe the dephasing time.

2.6 NV centers as quantum Processor

NV centers can also be a good candidate for quantum computing because of various reasons such as long spin coherence times, room temperature operation, optical addressability and readout. As discussed earlier, the ground state has electronic spin $S = 1$, which behaves as a qubit or even a qutrit. Under ambient conditions, this spin state has both long transverse and longitudinal relaxation times. Because of its optical properties, it can be polarised into one $m_s = 0$ state, this is known as spin polarisation or spin initialization, with mw pulse spin can be coherently driven into other spin sublevels which is, called as spin manipulation and readout of the state can be done by optically detected magnetic resonance (ODMR).

When the electronic spin shows coupling with the nearby nuclear spins, such as ^{13}C, ^{14}N, ^{15}N through hyperfine interactions, these nuclear spins serve as long-lived quantum states as they are weakly coupled with the environment. As hyperfine coupling provides multiple levels, this electron-nuclear system can be realised as multi-qubit registers.

2.6.1 Quantum Gates

In NV center quantum gates are the combination of various pulse sequences: a laser pulse for initialisation, a microwave frequency for the manipulation of electronic spin, a radiofrequency for the manipulation of the nuclear spin and again for readout, a laser pulse is used. By applying different combinations of π, $\frac{\pi}{2}$ pulses and various other pulses, quantum gates can be realised.

2.6.2 Controlled-NOT Gate

Controlled-NOT(C-NOT) gate is a fundamental two-qubit gate, which, with other arbitrary single-qubit gates, forms a universal gate set. In this gate, one qubit acts as a control qubit and the other as a target. If the control qubit is 1, it flips the target qubit. Mathematically, it is defined as:

$$|c, t\rangle \rightarrow |c, t \oplus c\rangle \tag{2.13}$$

To realise this type of gate in NV centers, in general, electronic spin can act as control qubit with $m_s = 0$ as $|0\rangle$ and $m_s = \pm 1$ as $|1\rangle$ and nuclear spin as target qubit if $I = \frac{1}{2}$ then $m_I = -\frac{1}{2}$ *as* $|0\rangle$ *and* $m_I = \frac{1}{2}$ *as* $|1\rangle$. This gate is represented as $C_e - NOT_n$, if vice versa, it is represented as $C_n - NOT_e$

We consider a system of a single electron spin ($S = 1$) and a ^{13}C ($I = \frac{1}{2}$) nuclear spin as shown in fig 2.8, which can be defined as:

$$\mathcal{H} = DS_z^2 + \gamma_e B S_z + A_{\parallel} S_z I_z + A_{\perp}(S_x I_x + S_y I_y) \tag{2.14}$$

where symbols have their usual meaning as described before. In this system each m_s spin level splits into two sublevels as shown in fig 2.8 The eigenstates of this system can be represented as $|m_s, 0\rangle$ and $|m_s, 1\rangle$.

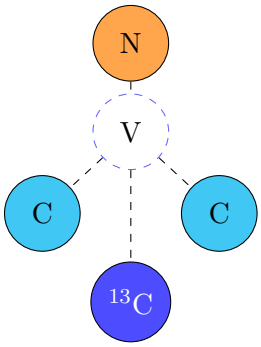

(a) Schematic of NV centerwith a ^{13}C nuclear spin.

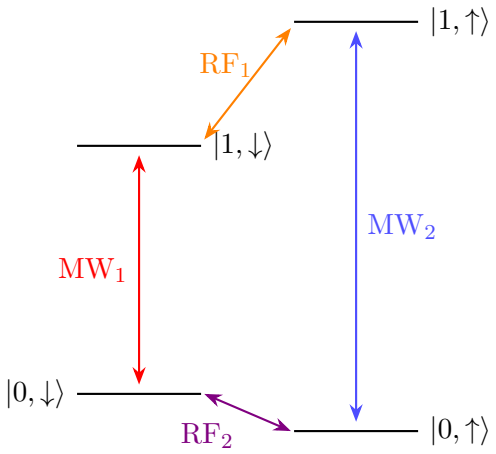

(b) Energy level diagram of NV-^{13}C. MW$_1$, MW$_2$: electronic spin transitions. RF$_1$, RF$_2$: nuclear spin transitions.

Figure 2.8: (a) Schematic of the NV-^{13}C spin system showing the nitrogen vacancy center coupled to a ^{13}C nuclear spin. (b) Energy-level diagram of the NV–^{13}C system showing the hyperfine levels for $m_s = 0$ and $m_s = \pm 1$, along with the microwave (MW) and radio-frequency (RF) transitions. Reference taken from [6].

For the implementation of the C-NOT gate, the first step is to initialize the state into $|0\rangle_e$, by the application of the green laser, since the green laser will polarise the electronic spin, so the nuclear spin will be an incoherent mixture. For polarisation of nuclear spin, methods described in [22], [4] and [23] can be used. After the polarisation, let's say that our system is in $|0\rangle$. We will apply a πpulse of MW$_1$ corresponding to $|00> \rightarrow |10>$ transition, which works as a X gate. Since our system is in $|10\rangle$, we will apply a π pulse of RF$_1$ which works as C-NOT gate here, as it will only work when our system is in $m_s = \pm 1$ that is, the controlled qubit is $|1\rangle$. So after applying Rf_1 our system is now in $|11>$ state.

For performing this operation discussed above, we should know what are the RF

pulses are required for the respective transition. AS for microwave pulse, we do ODMR and spin rabi oscillation, similarly we can do Electron-Nuclear Double Resonance and nuclear spin rabi oscillation as shown in fig 2.9, for RF pulse [4].

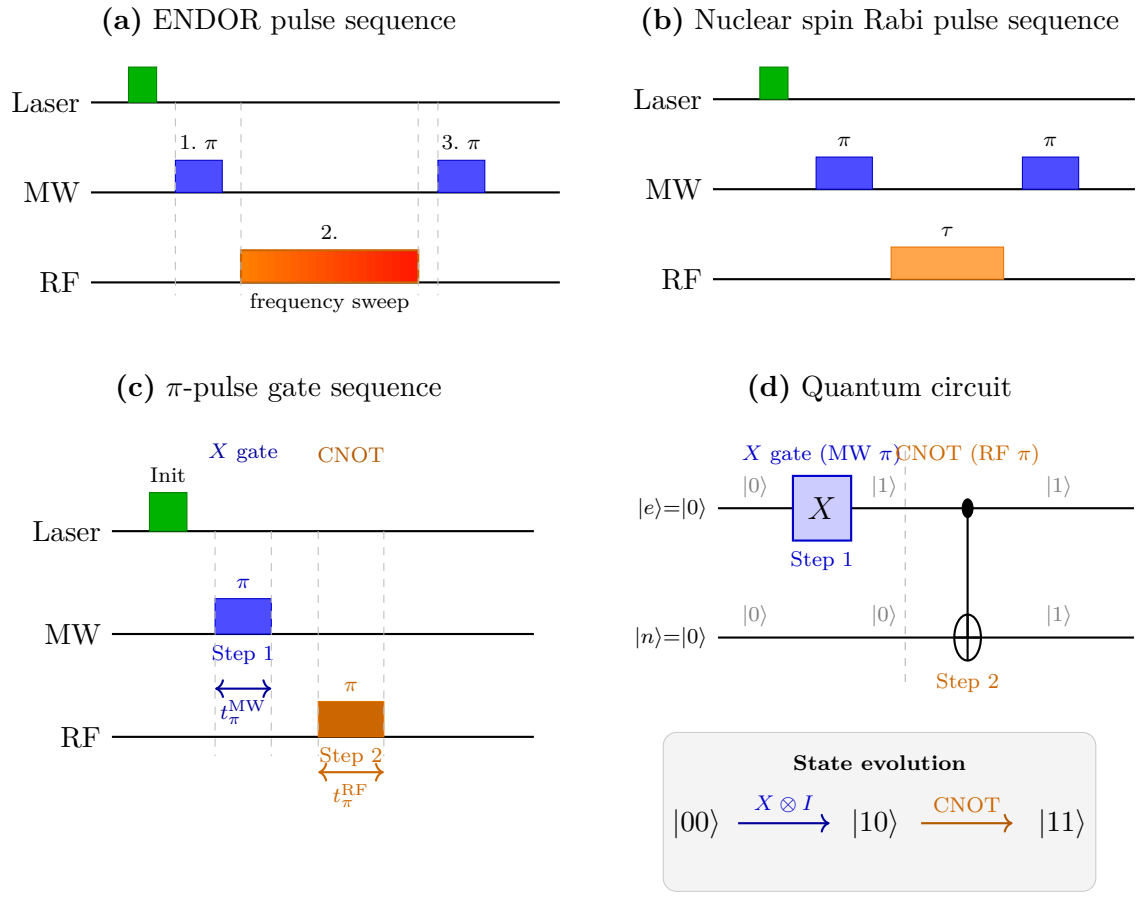

Figure 2.9: NV-centerexperiment pulse sequences and quantum circuit. **(a)** ENDOR sequence is used to get the resonance frequency for nuclear spin transitions: laser init, MW π pulse (step 1), frequency-swept RF pulse (step 2), second MW π pulse (step 3). **(b)** Nuclear spin Rabi sequence is done for optimisation of pulse duration for Rf : laser init, MW π pulse, RF τ pulse (variable duration), second MW π pulse. **(c)** Quantum gate π-pulse sequence: laser init, MW π pulse (Step 1, X gate, t_π^{MW}), RF π pulse (Step 2, CNOT, t_π^{RF}). **(d)** Equivalent quantum circuit with state evolution $|00\rangle \xrightarrow{X\otimes I} |10\rangle \xrightarrow{\mathrm{CNOT}} |11\rangle$.

Chapter 3

Methods

3.1 Confocal microscope and Control system

Confocal microscopy is an established method which is used to acquire images with high spatial resolution by eliminating of out-of-focus light through a spatial pinhole. In this method, a focused laser beam of small diffraction-limited spot size excites a certain volume within the sample, and subsequently, the emitted fluorescence is selectively collected at the focal plane of the objective lens.

In this study, confocal microscopy proves to be a valuable tool for spatially isolating NV centers in diamond with high spatial resolution. In addition to imaging of the sample surface, it allows selective excitation and addressing of individual NV centers, which is indispensable in experiments with coherent manipulation of spins.

A custom-made confocal microscope, schematically illustrated in Fig. 3.1, was constructed for all experiments performed in this work. It is capable of operation in both CW and pulsed regimes of laser excitation of the samples, making it suitable for acquisition of ODMR and time-resolved spectra of spin dynamics of NV centers.

In general, the design of the confocal microscope can be divided into three main parts: (i) the laser excitation, (ii) fluorescence detection, and (iii) control/synchronization systems.

3.1.1 Excitation Path

To optically excite the nitrogen-vacancy centers, a continuous wave laser at 515 nm (iBeam smart from TOPTICA Photonics) is used with maximum output power up to 150 mW. Laser power can be precisely regulated by using the software of iBeam smart control.

For reducing the size of the laser beam to about 1mm, a telescope configuration with two plano-convex lenses of 100 mm and 50 mm focal lengths are used. The aim of the telescope system is to shrink the laser beam to fit the aperture of the acousto-

optic modulator (AOM), it is being driven by RF pulses from Urukul, discussed in detail in the control system section. The latter is used for pulse laser operation. Upon application of an RF signal to the AOM crystal, periodic modulation of the refractive index is achieved, leading to the formation of a diffracting grating structure with several orders of diffraction. During optimization, the first order of diffraction contains maximal optical power of about 75 % of the input laser power. Other orders of diffraction are blocked out by using an iris.

The first-order beam is then guided through an optical path by mirrors (M1 and M2). Proper alignment must be made before the light enters the objective of the microscope. It is important to make sure that neither the excitation light nor the detected signal interacts with the microscope objective walls in any way.

A dichroic mirror is installed in the path of the objective as shown in fig 3.1 for distinguishing between excitation and collection optical paths, since the dichroic mirror reflects the green excitation light while passing the fluorescence produced by the NV centers. A 100x microscopic objective (EC Epiplan 100x objective) having a numerical aperture (NA) 0.85 and a field of view of about 0.23 mm is used for focusing the laser beam onto a diffraction-limited spot inside the diamond.

The diamond sample with NV centers is attached to a microwave antenna directly and can be optically excited at the same time. And the microwave antenna is mounted on an X-Y piezo stage, which allows for precise spatial scanning of the sample and addressing of single NV centers in the confocal microscope setup.

3.1.2 Detection Path

After exciting the NV centers with the green laser, the emitted fluorescence is gathered by the same microscope objective with high numerical aperture. The collected light travels along the optical path as depicted in fig 3.1, passing through a dichroic mirror that separates the excitation and emission paths by reflecting the excitation light but passing the fluorescence.

Next, the fluorescence is filtered spectrally by placing a band-pass filter centered around 633 nm with a band of 40nm. Filtering ensures that only the fluorescence from the NV^- center passes through; it blocks any background signals, such as the excitation beam and fluorescence from the NV^0 centers.

The filtered fluorescence is then focused by a 50 mm plano-convex lens to a 50 µm diameter pinhole. This pinhole serves as a spatial filter by rejecting out-of-focus light, thus permitting confocal detection that improves spatial resolution.

Finally, the fluorescence is focused onto the end of a multimode optical fiber by the lens and is conducted by the fiber to the detector, namely a single photon avalanche diode. The detected photons are then measured by a time tagging device to analyse

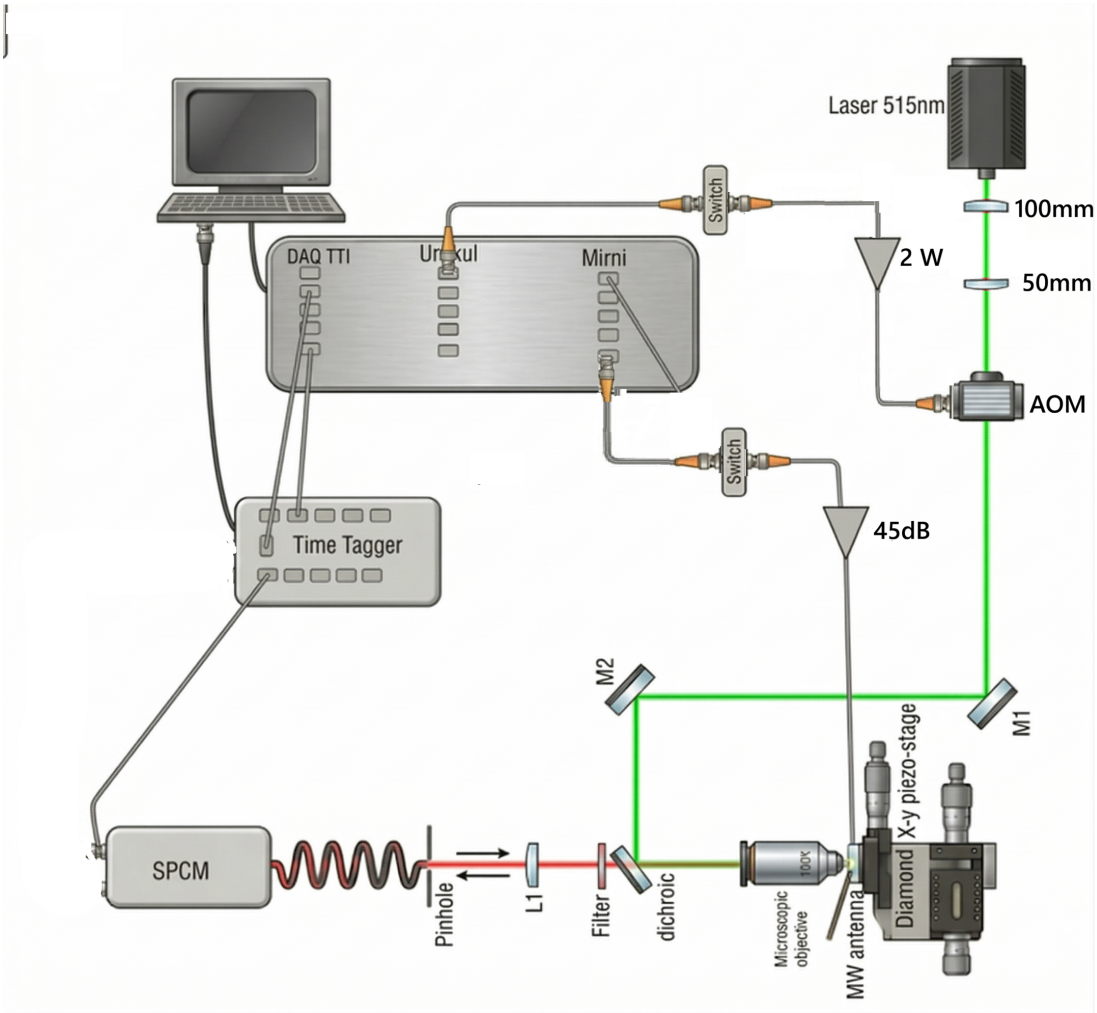

Figure 3.1: Schematic of the confocal microscope setup used for the experiment.

the timing information of the fluorescence.

3.1.3 Control System

The control system controls critical experimental variables such as laser excitation timing, microwave frequency sweeps, microwave pulse timing, and the creation of complex sequences of pulses. In this regard, we use Sinara, which is an open-source hardware that is specifically designed for performing quantum experiments. The Sinara system consists of various modifiable units, including Mirny for generating microwave signals, Urukul for controlling RF frequencies, TTL modules for performing digital input/output processes, and ADC modules for acquiring data from signals.

To program and control the Sinara hardware, we use the ARTIQ (Advanced Real-Time Infrastructure for Quantum Physics). ARTIQ is an open-source software framework specifically developed for quantum information and quantum optics applications. With the help of this framework, a person can design experimental sequences based on

the Python language. After designing a sequence, ARTIQ translates it to the FPGA device and executes it.

The inclusion of FPGA device results in the ability of ARTIQ to perform a sequence of instructions deterministically on hardware. Therefore, by executing the instructions on the FPGA, nanosecond-scale timing can be achieved.

Figure 3.2: SINARA Hardware

Mirny: Microwave Synthesizer

For the control of the electronic spin of the NV center, it is necessary to have a very accurate and reliable microwave signal. In order to do that, we use the Mirny module, a frequency synthesizer working in the microwave range up to 4 GHz, which produces up to 52 bits of frequency resolution from 53 MHz. It is operated via ARTIQ software, allowing the production of microwave pulses in a precisely defined time interval.

The maximum output power of the Mirny module is about +5 dBm. However, it is not enough to produce an efficient signal for spin manipulation in our experiment. In order to increase the output power of the microwave signal, we use a microwave power amplifier, which is ZHL-16W-43+, made by Mini-Circuits. It provides amplification of the input signal by increasing its output power up to 42 dBm (16 W), which is checked by a calibrated power meter.

Thus, the amplified microwave signal is fed to the microwave antenna and is responsible for manipulating the spin state of the NV center.

We can distinguish two main operational regimes of the Mirny module. First, it is used to make frequency sweeps of the microwave signal in order to acquire the ODMR spectrum of the NV center. The second regime implies generating precisely time-controlled microwave pulses for spin manipulations, including Rabi oscillations and Ramsey interferometry experiments.

Microwave antenna

In order for efficient control of the NV spin state, it is necessary to provide a sufficiently powerful oscillating transverse magnetic field (B_1) near the place where the NV center resides in the diamond crystal lattice. In order to accomplish this, a microwave antenna, as shown in fig. 3.3, is used to transmit the microwave signal from the Mirny module to the diamond sample.

In our experiment, a specially designed single-port microwave antenna is used that operates at a resonance frequency of ~ 2.87 GHz. This corresponds to the zero-field splitting between the ground states of the NV center, which allows the microwave signal to resonantly excite the spin transition. The diamond is placed at the center loop to provide maximum intensity of the microwave magnetic field near the NV center. It also radiates at different frequencies, which allows us to perform various experiments with different microwave frequencies, such as excited-state ODMR and different quantum gates.

This was achieved by characterising the antenna with the vector network analyzer (VNA) and measuring the magnitude of the return loss (S_{11}) of ~ -10 dB. The latter means an impedance matching of 10% reflected power. For details regarding the fabrication and simulation of the MW antenna refer to "Compact and portable NV Center Magnetometer for Field Application" by Dipansh Raput.

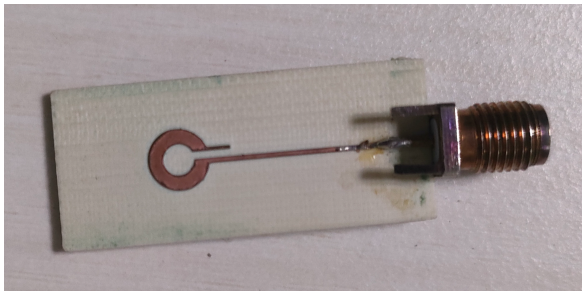

Figure 3.3: Microwave antenna used for delivering the microwave signal to the sample.

Urukul: Direct Digital Synthesizer (DDS)

In a similar fashion, a precise control of the laser excitation is mandatory for the successful execution of the experiment. To achieve this aim, aom is driven using the Urukul module – a multichannel direct digital synthesizer (DDS) module that is part of the Sinara ecosystem. The Urukul module is designed to generate RF signals with frequencies ranging from 1 MHz to 400 MHz, with a resolution of 8 µHz. Every channel can deliver an output power of up to +10 dBm (10 mW).

The Urukul module generates a highly accurate and tunable RF signal, which is necessary to stimulate the acousto-optic modulator (AOM) required for pulsed laser

control. Specifically, we use the ATM-2001A1 produced by IntraAction Corp.. In order to operate efficiently within the Bragg diffraction regime, the AOM must be driven by an RF signal with a frequency of about 200 MHz and a power of 600 mW.

The Urukul power output is not sufficient to be used directly on the AOM, hence the RF signal is amplified by a 2-W RF amplifier. Before amplification, there is an attenuation of 4.5 dB in the digital domain by the ARTIQ controller. The attenuation helps in controlling the amount of RF power being sent to the amplifier and ensures the AOM works at an optimal level of RF power.

In optimized conditions, the efficiency of diffraction from the AOM into the first-order beam is approximately 75

TTL Digital I/O

For achieving accurate synchronization among all parts of the experiment, conventional Transistor–Transistor Logic (TTL) output units are used. Using the ARTIQ–Sinara platform, these TTL units ensure deterministic digital manipulation with sub-nanosecond timing accuracy and rapid switching rates. High temporal accuracy is necessary for synchronization between various parts of the experiment, such as laser pulses, microwave manipulation, and measurement protocols.

Several TTL outputs are employed to create and regulate various pulse trains, thus providing versatility in designing the experimental protocol. The particular timing schemes and pulse trains used in the current study will be explained in the next sections.

3.2 Confocal Raster Scanning of NV Centers

3.2.1 Principle of Confocal Microscopy

As discussed at the start of this chapter, the confocal microscope is a high-resolution optical imaging system with which one can spatially resolve the fluorescence from the sample by reflecting out-of-focus light.

A tightly focused laser beam is used to excite the diamond with a high numerical aperture objective lens. Due to diffraction, the focal spot has a finite size, which limits the spatial resolution of the system The lateral resolution is given as:

$$\delta r \approx \frac{0.61\lambda}{\mathrm{NA}} \tag{3.1}$$

and the axial (depth) resolution is given by:

$$\delta z \approx \frac{2n\lambda}{\mathrm{NA}^2} \tag{3.2}$$

where λ is the excitation wavelength, NA is the numerical aperture of the objective lens, and n is the refractive index of the medium.

3.2.2 Raster Scanning Method

A two-dimensional image of the diamond to map NV-centers is generated using a raster scan method. In this method, the sample is mounted on a piezo-electric nanopositioning. stage and then a scan is carried out in a line-by-line manner as shown in fig 3.4, in which the x-axis serves as the fast axis and the y-axis as the slow scanning axis.

For each fixed Y position, the X position is varied across the scan range. After completing one line, the Y-axis moves to the next line, and this process is repeated to scan the complete area. At each pixel (x_i, y_j), the fluorescence signal is recorded over a fixed integration time.

$$I(x_i, y_j) \propto N_{\text{photons}} \tag{3.3}$$

where N_{photons} is the number of detected photons.

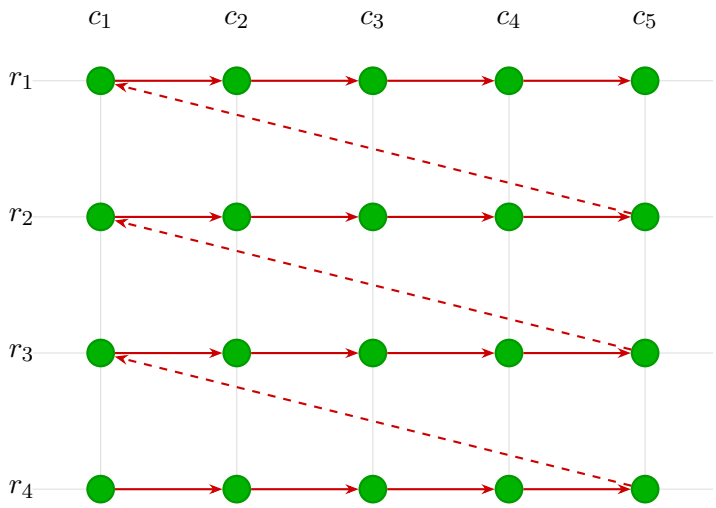

Figure 3.4: Grid scan pattern: solid arrows indicate horizontal traversal within each row; dashed diagonal arrows indicate long-range skip connections across rows. (This image was created by taking a refernce from swabianinstruments.com)

3.2.3 Experimental Scheme

Position Control

A x-y piezo-electric stage was made for this experiment, as shown in fig 3.5 using two piezo discrete round piezo stacks (PK25FA2P2) from Thorlab were used, which can be controlled by Thorlabs MDT694B, and can be controlled through a Python

interface. This stage was calibrated by michelson interferometer, from which it was found that the displacement of the stage is not a linear function of a voltage, it also follows to different paths while moving forward and backwards, as shown in fig. 3.6.

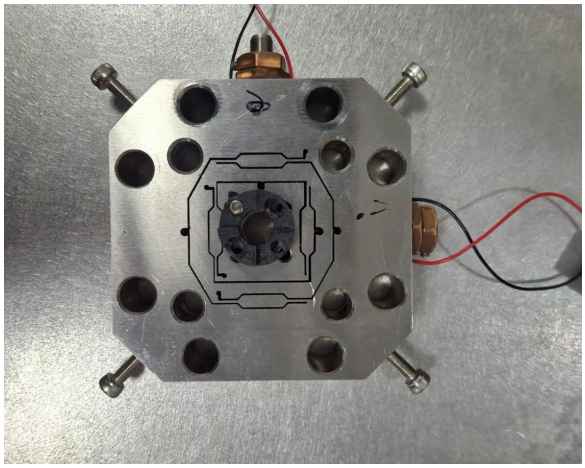

Figure 3.5: Pizeo-stage callibrated.

To make sure that the scan is linear, a unidirectional scanning method was used. The displacement in the forward direction as a function of voltage is given as follows:

$$D(V) = -1.29V^3 - 12.17V^2 + 1046.1V + 60.6 \tag{3.4}$$

where $D(V)$ is the displacement in nanometers, and V is the applied voltage.

The following procedure was used to take a linear scan:

1. The scan starts by setting a fixed position in y-axis first.
2. Then scan the x-axis in the forward direction only in such a way, let's say the whole travel of x-axis is $8\mu m$ but we want to scan just $5\mu m$, so what we do is to collect data for $5\mu m$ only and then moves to the end of its full range, i.e. $8\mu m$ without collecting data and then come back using the backward path.
3. As can be seen in the curve, after coming back, it shows a small displacement on the y-axis also, so to make sure it comes back to the same (x, y) position from where it started, a displacement of 728nm is given on the y-axis.
4. Then, to move to the next line, a displacement in y-axis is given again, and the above steps are repeated.

Since the fluorescence was detected using a single photon counting module(SPAD), which was connected to the swabianin time tagger. Both the swabianin time tagger and the Thor lab pizeo controller MDT694B can be controlled through python, so position control and data acquisition can be handled by a single code file, without the

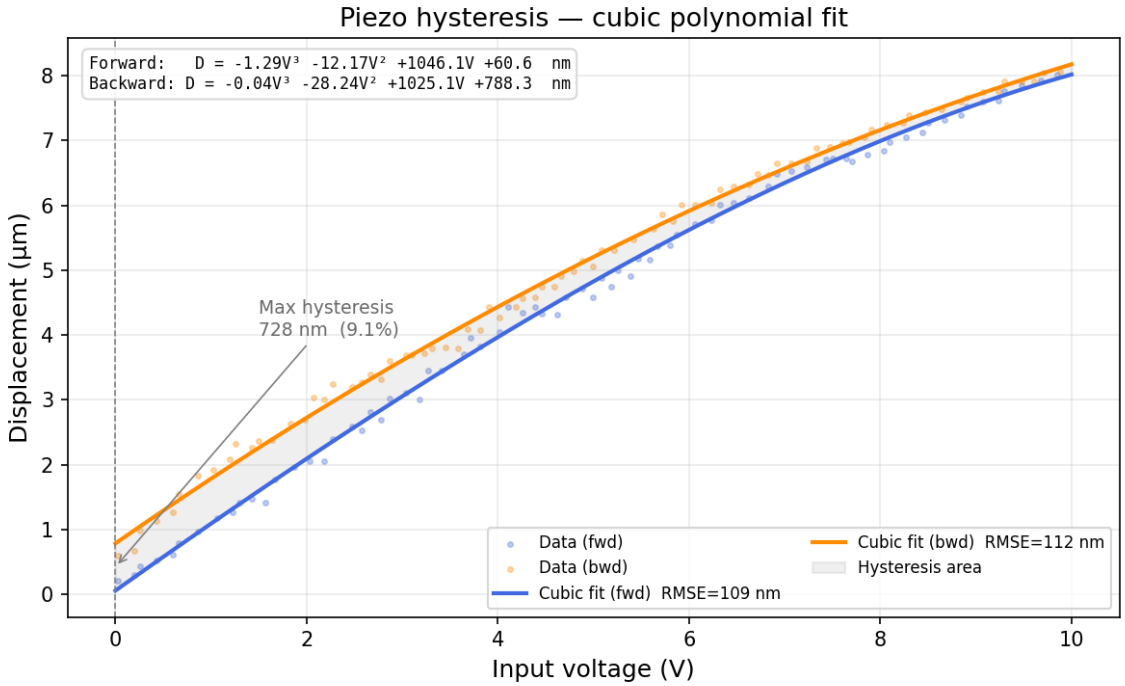

Figure 3.6: Pizeo-hysteresis.

need for a TTL signal to trigger one or the other. As a result, a fully synchronized confocal image was generated.

3.3 Experimental Protocols for ODMR

As discussed in the previous chapter, the NV center has a triplet ground state with spin sublevels $m_s = 0$ and $m_s = \pm 1$, which are split by a zero-field splitting (ZFS) of approximately 2.87 GHz due to spin-spin interactions.

After the application of a magnetic field, the $m_s = \pm 1$ sublevels further split due to the Zeeman effect, allowing for selective addressing of individual spin transitions. To identify the resonance frequencies of these transitions, optically detected magnetic resonance (ODMR) techniques are employed.

Three different methods of ODMR are used in this work: continuous wave ODMR, pulsed ODMR, and differential ODMR, they follow the same principle for measuring the splitting, by measuring the changes in fluorescence intensity under optical excitation while applying microwave radiation to manipulate the spin state of the NV center.

As described in section isc, a general ODMR measurement protocol is defined by a logical sequence of operations:

1. **Spin Initialization:** The NV center is optically pumped into the $m_s = 0$ state using a green laser (is our case a 515 nm). This process polarizes the spin state

by the ISC system.

2. **Spin Manipulation:** A microwave field is applied to the NV center, sweeping across a range of frequencies around the zero-field splitting. When the microwave frequency matches the energy difference between the spin sublevels, transition between the $m_s = 0$ and $m_s = \pm 1$ states takes place.

3. **Readout:** The fluorescence emitted by the NV center is recorded as a function of the microwave frequency. Due to the spin-dependent fluorescence, the $m_s = \pm 1$ states exhibit reduced fluorescence compared to the $m_s = 0$ state because of non-radiative decay pathways as discussed earlier. As a result, a dip in the fluorescence intensity is observed at the resonance frequency, indicating the occurrence of spin transitions.

3.3.1 Continuous-Wave ODMR (CW-ODMR)

In CW-ODMR mode, the three steps, spin initialization, Spin Manipulation, and readout, are done simultaneously. Continuous excitation of the NV center by the green laser keeps it in its steady state, which selectively prepares it for excitation to the $m_s = 0$ sublevel. At the same time, an MW field induces transitions between the $m_s = 0$ sublevel and the $m_s = \pm 1$ sublevels.

In our current experiment, the MW frequency sweep is done in discrete steps of approximately 1 MHz within the range of a few hundreds of MHz (e.g., 2.7 to 3.0 GHz). At each sweep frequency step, the fluorescence intensity is measured for a fixed period ($\sim$1 ms).

Experimental Implementation using ARTIQ

For the implementation of the CW-ODMR, a pulse sequence as shown in fig 3.7 is designed using the ARTIQ control system. The sequence is structured to ensure that the laser excitation, microwave control, and data acquisition are precisely synchronized.

1. **Continuous Optical Pumping** AOM is being driven by a digital Synthesizer (DDS), which provides 200MHz RF excitation. According to the CW-protocol, the AOM is enabled at the start of the sweep, and is kept active during the whole pulse sequence, which means that the 515nm laser is continuously exciting the NV center and polarising it into $m_s = 0$ during the entire measurement.

2. **Microwave sweeping** For microwave sweeping, the Mirny is coded in such a way that it takes discrete frequency steps with a resolution of 1MHz, sweep starts from frequency f_1 (2.7 GHz) to f_n (3.0 GHz) which can also be varied, and at each frequency step, the fluorescence is measured for a fixed integration time

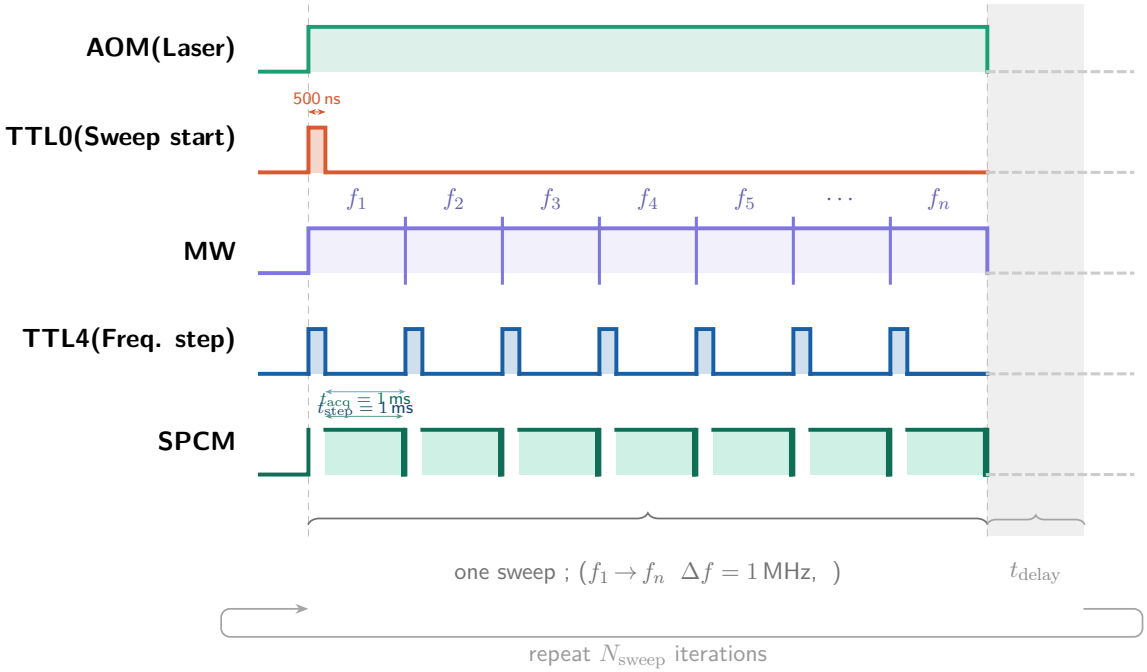

Figure 3.7: CW-ODMR pulse sequence with synchronized frequency-step triggering. TTL0 marks the sweep start, TTL4 defines frequency bins, and SPCM counts photons for each step.

of 1ms. ARTIQ has some settling time after each frequency step, to make sure that the microwave frequency is stabilized before the fluorescence measurement starts, some delay is given. This is crucial for accurate measurement of the ODMR spectrum, as any instability in the microwave frequency could lead to inaccurate determination of the resonance conditions. The settling time allows the system to reach a steady state after each frequency change, ensuring that the measured fluorescence intensity accurately reflects the response of the NV center to the applied microwave field at that specific frequency.

3. **Data Acquisition and Sycnhronization** This is a crucial step to make sure that the fluorescence counts are correctly associated with the corresponding microwave frequencies. The fluorescence signal is collected using a single-photon counting module(SPCM), which sends the NIM pulse to a time tagger to record the arrival times of the photons. To synchronize the data acquisition with the microwave frequency steps, TTL signals are generated by ARTIQ and are connected to the Time Tagger to ensure precise timing control. Two TTLs were used in this experiment: one is TTL0 which is used to track the number of sweeps, and the other is TTL4, which is used to trigger the Time Tagger for readout at the start of each frequency step.

This whole sequnece in repeated multiple times, a variable number of sweeps (e.g., $N_{\text{sweep}} = 20$) is added in the loop, and every new sweep is averaged to improve the

signal-to-noise ratio of the resulting ODMR spectrum. The final output is a plot of fluorescence intensity versus microwave frequency, where dips indicate the resonance frequencies corresponding to spin transitions in the NV center. Some time delay is given after every sweep to allow the system to relax by switching off microwave fields. This is important to prevent any unwanted heating effects and to ensure that each sweep starts with the NV center in a well-defined initial state.

3.3.2 Pulsed Wave ODMR

In Pulsed wave ODMR, a pulse sequence is designed such that all three steps are performed sequentially rather than simultaneously. First, a green laser is pulsed by using AOM to initialize the spin state into the $m_s = 0$ state, then it is followed by a microwave pulse to manipulate the spin state, and then a readout pulse to measure the fluorescence intensity. This technique is more efficient than CW-ODMR as it reduces the power broadening effects and allows for more precise control over the spin state, which leads to sharper resonance features in the ODMR spectrum. Experiments like Rabi oscillations, Ramsey fringes, and spin echo measurements can be performed using pulsed ODMR to extract different spin properties such as π pulses, dechorence time and can design Quantum gates in this mode.

Experimental Implementation using ARTIQ

A pulse sequence was developed as shown in fig 3.8, where the laser pulse is used for initialization, followed by a microwave pulse for spin manipulation, then a readout pulse to measure the fluorescence intensity and then different TTL signals for synchronization. The timing of each pulse can be adjusted to optimize the signal and minimise any unwanted effects such as power broadening or heating of the NV center. The sequence goes as follows:

1. **Spin Initialization**: First step is to optically pump the NV center into the $m_s = 0$ state, for this, a pulse of green laser is given by using AOM, the duration of the pulse can be optimized to ensure the polarization typically, the pulse duration is in the range of a few microseconds (3-6μs).For our experiment, it was optimized to 4μs. This pulsing of the laser using AOM is done by programming the ARTIQ to generate a TTL pulse by the Urukul channel that controls the AOM, allowing for precise timing of the laser excitation.

2. **Spin Manipulation**: After optically pumping the spin state to the $m_s = 0$ state, the next step is to manipulate the spin state using a microwave pulse. The microwave pulse of f_i is generated by the Mirny module, which is programmed to produce a pulse of specific duration and power. Generally, the duration of

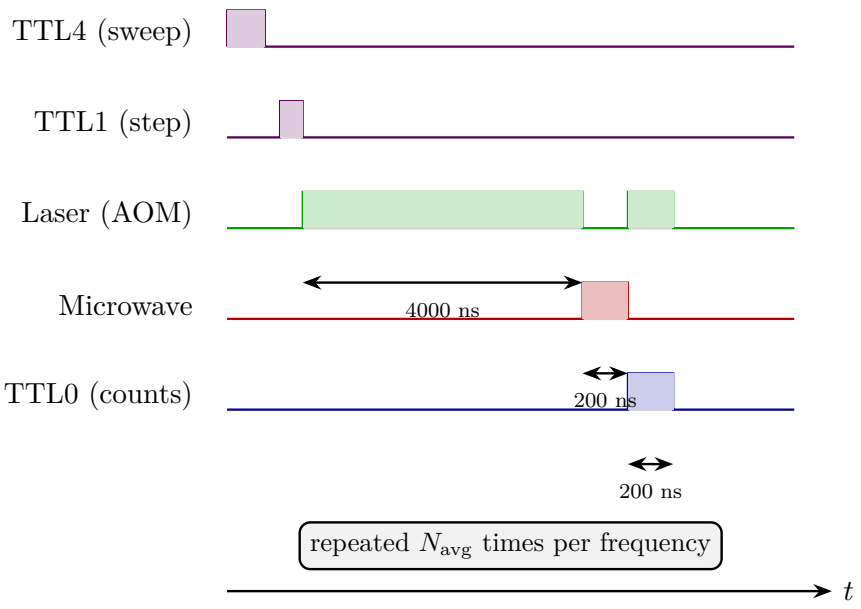

Figure 3.8: Pulsed ODMR sequence implemented in ARTIQ. Each frequency point consists of laser initialization, microwave excitation, and fluorescence readout. The readout is performed simultaneously with laser illumination, and the sequence is repeated multiple times for averaging.

the microwave pulse is a π pulse, which corresponds to a full population transfer between the $m_s = 0$ and $m_s = \pm 1$ states at resonance f_i. The duration of the π pulse can be calculated by the Rabi oscillation. But in this experiment, the duration of the microwave pulse was optimized manually by varying the pulse length; a pulse length of $200\mu s$ was given in this experiment.

3. **Readout**: After the microwave pulse, a readout pulse is applied to measure the fluorescence intensity. In this step, the green laser is again pulsed to excite the NV center, , first 300-400 ns are crucial as this corresponds to the Inter-system Crossing(ISC) relaxation time, and this makes the difference in the fluorescence intensity between the $m_s = 0$ and $m_s = \pm 1$ states, so the readout pulse is designed to capture this time window to maximize the contrast in the ODMR spectrum.

4. **Synchronization**: Three different TTL signals from ARTIQ-Sinara are used to synchronize the different parts of the experiment discussed as follows:

   - **TTL4 (Sweep Sync Marker)**: TTL4 is used to synchronize the start of each sweep; it is connected with the time tagger channel 3, and it gives a trigger to the time tagger at the start of each sweep, this TTL is crucial for multiple sweeps and averaging, as it allows the time tagger to align the photon counting data with the corresponding microwave frequency steps across multiple sweeps.

- **TTL1 (Frequency Step Marker)**: TTL1 is used to mark the frequency steps; it is connected to time tagger channel 1, and it gives a trigger to the time tagger when the frequency is changed to the next step, because of which the time tagger moves to next bin for counting the photons, this allows for precise correlation between the microwave frequency and the corresponding fluorescence intensity.
- **TTL0 (Gate)**: TTL0 is used as a gated signal for photon counting; it is connected to channel 4 of time tagger, and it makes sure that photon counting happens only in this window, which is helpful in reducing the background noise.

Note: For each microwave frequency point during a single sweep, the pulse sequence is repeated multiple times to bin sufficient photon counts and improve statistical accuracy and contrast in this experiment it was done 1000 times. In addition, multiple sweeps are performed and averaged to further improve the signal-to-noise ratio.

3.3.3 Differential ODMR

This technique is more advance, accurate and reliable as compared with other odmr methods, with this we can overcome the fluctuations caused by the laser power drift, background fluorescence and environmental noise such as strain and temperature [24]. In this technique, one can extract information like splitting of dips, resonance peaks, more accurately.

In this method, instead of measuring the signal at f_i, it is recorded two points which are slightly detuned by $\pm\frac{\Delta f}{2}$ from f_i. The difference in the fluorescence of these two points is plotted at f_i. The signal obtained by this method is directly proportional to the slope of the ODMR spectrum [25].

The curve obtained from this method is no longer a Lorentzian in nature, instead a dispersive(derivative-like) line shape with zero-crossing at the resonance frequency, which makes it more useful for identification and tracking of resonance positions. This technique is related to lock-in detection, which is discussed in [26].

Mathematical Derivation

Let the fluorescence intensity as a function of microwave frequency be denoted by $I(f)$. In the differential measurement scheme, two intensities are recorded:

$$I_{\pm} = I\left(f \pm \frac{\Delta f}{2}\right) \tag{3.5}$$

The differential signal, ΔI, is defined as the difference between these two points:

$$\Delta I = I_+ - I_- \tag{3.6}$$

To interpret this signal in terms of the underlying spectral profile, we apply a first-order Taylor expansion to $I(f)$ around the central frequency f:

$$I\left(f \pm \frac{\Delta f}{2}\right) \approx I(f) \pm \frac{\Delta f}{2}\frac{dI}{df} + \frac{1}{2}\left(\frac{\Delta f}{2}\right)^2 \frac{d^2 I}{df^2} + \mathcal{O}(\Delta f^3) \tag{3.7}$$

Substituting these expansions into the expression for ΔI, the even-order terms (including the background intensity $I(f)$) cancel out, yielding:

$$\Delta I \approx \left[I(f) + \frac{\Delta f}{2}\frac{dI}{df}\right] - \left[I(f) - \frac{\Delta f}{2}\frac{dI}{df}\right] \tag{3.8}$$

$$\Delta I \approx \Delta f \cdot \frac{dI}{df} \tag{3.9}$$

The resulting signal is therefore directly proportional to the slope of the original ODMR line shape. This linearity near the resonance frequency significantly improves the robustness of the system against external noise sources that shift the global intensity without altering the local gradient.

Table 3.1: Comparison between Standard ODMR and Differential ODMR techniques.

Feature	**Standard CW-ODMR**	**Differential ODMR**
Spectral Line Shape	Lorentzian (Dip/Peak)	Dispersive (First-Derivative)
Signal Source	Absolute Intensity $I(f)$	Intensity Difference ΔI
Resonance Identification	Minimum/Maximum Point	Zero-Crossing Point
Sensitivity to Power Drift	High (Baseline shifts)	Low (Common-mode rejection)
Tracking Performance	Low (Zero slope at center)	High (Maximum slope at center)
Primary Application	Spectral Characterization	Precision Sensing & Tracking

Experimental Implementation using ARTIQ

A pulse sequence was developed for this as shown in fig 3.9. Experimental implementation is almost same as that of PW-ODMR, the key difference is lies in frequency modulation, TTL trigger to differentiate between $+\frac{\Delta f}{2}$ and $-\frac{\Delta f}{2}$ and how the data is being processed by time tagger.

The Sequence is as follow:

1. **Frequency Modulation** After spin intialization which is similar to PW-ODMR, the modulation parameter Δf is defined. For each frequency point f_i, two measurements are done, in first cycle, a microwave pulse of $f_i - \frac{\Delta f}{2}$ is given by Mirny synthesizer, and similarly, in the next cycle, a microwave pulse of $f_i + \frac{\Delta f}{2}$

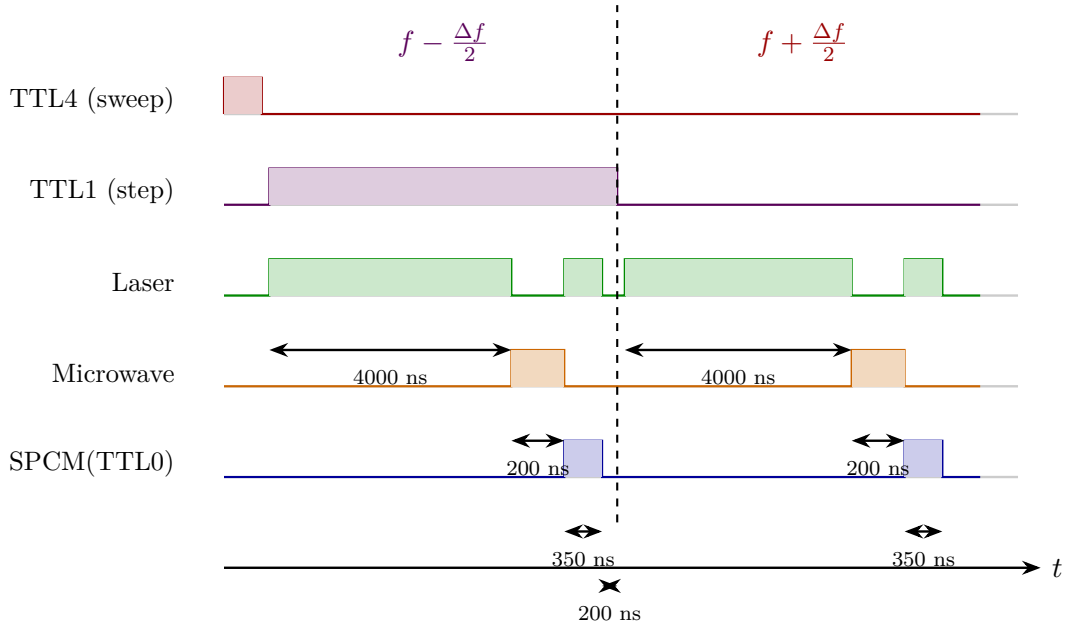

Figure 3.9: Differential ODMR pulse sequence. Two measurements at $f \pm \frac{\Delta f}{2}$ are performed per cycle. TTL1 encodes the frequency branch, TTL4 marks the sweep start, and fluorescence readout occurs simultaneously with laser illumination.

is given. For optimizing the parameter Δf different values were used, and it was observed that the Δf equal to the linewidth of the ODMR obtained in the PW Mode gives the best result, which in this case was 10 MHz

2. **Synchronization** Three different TTL signals from ARTIQ-Sinara are used to synchronize the different parts of the experiment discussed as follow:

   - **TTL4** is being used in the same way as it was being used in PW-ODMR for synchronizing the start of the sweep and for averaging different sweep.
   - **TTL1** is being used to synchronize the frequency modulation. When time tagger detects the rising edge of of the trigger, it bins the data for $f_i - \frac{\Delta f}{2}$ and when a falling edge is detected it starts to bin the data for $f_i + \frac{\Delta f}{2}$. And when it again detects the rising edges it move to $f_{i+1} - \frac{\Delta f}{2}$ bin.
   - **TTL0** is used in the same way as PW-ODMR for a gated signal for photon counting.

NOTE: For each microwave frequency point during a single sweep, the pulse sequence is repeated multiple times to bin sufficient photon counts and improve statistical accuracy and contrast in this experiment it was done 1000 times. In addition, multiple sweeps are performed and averaged to further improve the signal-to-noise ratio.

Chapter 4

Results and Discussion

4.1 Confocal Image

The confocal scan of the diamond was taken as described in the section 3.2. Figure 4.1 shows the $7\mu m$ X $7\mu m$ confocal scan, fluorescence at a single point was recorded for a time period of 1 millisecond. The variations in count rate ranged from 1300 to 1700 count/ms, as shown in the colour scale.

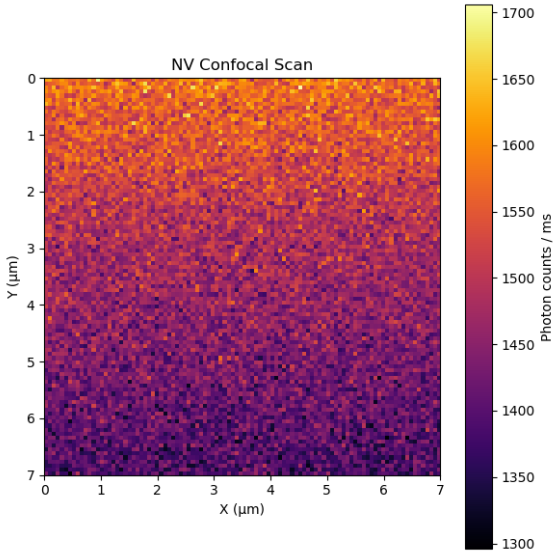

Figure 4.1: Confocal scans hows the $7\mu m$ X $7\mu m$ scan with step size of 200 .

It can be observed that no single NV's were present in the region of scan, several different regions were scanned but no single NV's were found. The diamond sample used has a good level of doping with some spatial inhomogeneity.

4.2 Excited state and Ground state zero field splitting

As it was discussed in the section 2.2.2, the NV centres exhibit zero field splitting in both excited state and the ground state, to show this, an ODMR spectrum was taken by using the pulse sequence discussed in the section 3.3.2 with the microwave sweep range from the 1.3 GHz to 3 GHz with step size of 2 MHz.

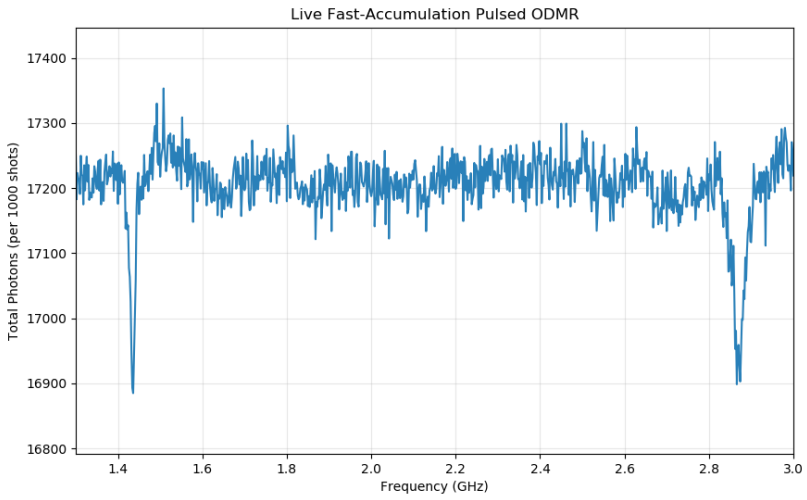

(a) Zero-field splitting in ground and excited states

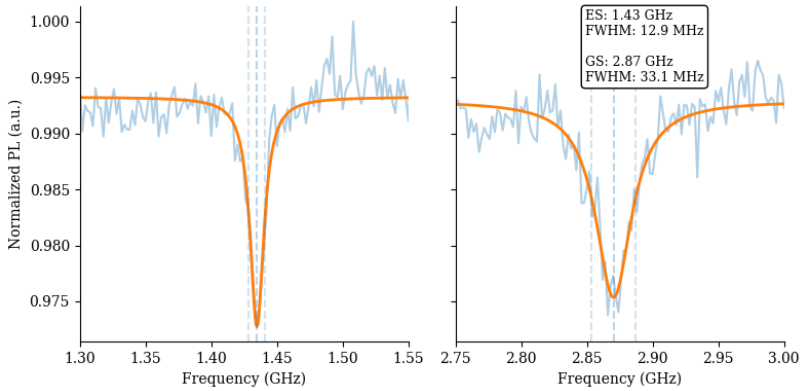

(b) (Zoomed in Lorentzian fit

Figure 4.2: Comparison of energy level structure and experimental/result plot.

Two resonance dips at 1.43 GHz and 2.87 Ghz were observed in the ODMR spectrum due to zero field splitting, corresponding to the excited state (D_{es}) and Ground state(D_{gs}), respectively. This confirms the physics of the Intersystem crossing(ISC). The excited-state ODMR can be helpful in studying the excited-state-level anti-crossing (ESLAC). In this condition, the electron-nuclear spin mixing takes place, which efficiently polarises the nuclear spin under optical excitation [23].

4.3 Resolving the Resonance Frequency

For the coherent manipulation of spins, having Knowledge about the resonance frequency is important in quantum computing. In NV centers, the resonance frequency is given by the energy difference between the spin sub-levels participating in the transition $m_s = 0 \rightarrow m_s = \pm 1$. Using microwaves at this exact resonance frequency allows driving coherent transitions between the two spin sub-levels, thus implementing π and $\pi/2$ gates in quantum computing.

The accuracy of the resonance frequency knowledge is very important to make high-quality operations with quantum states. In case of the resonance frequency detuning, the operations will not work properly and result in errors and inaccuracies. Knowing precisely this value is also necessary for using techniques that include Rabi oscillation, Ramsey interferometry, and spin echo to evaluate the coherence of the qubit states.

To experimentally determine these frequencies Optically detected magnetic resonance is done. As discussed in section 3.3, three different methods can be used to perform ODMR. Here all three methods are experimentally implemented and discussed :

4.3.1 Continuous Wave-ODMR

Continuous wave ODMR is the simplest technique. As described in section 3.3.1, in this method, continuous illumination, microwave sweeping, and fluorescence detection are done simultaneously. Fig 4.3 shows the results of CW-ODMR, the dip at 2.87 GHz in Fig 4.3a shows the resonance frequency required for the transition from $m_s = 0 \rightarrow m_s = \pm 1$, when no magnetic field is applied this is also know as zero field splitting(ZFS).

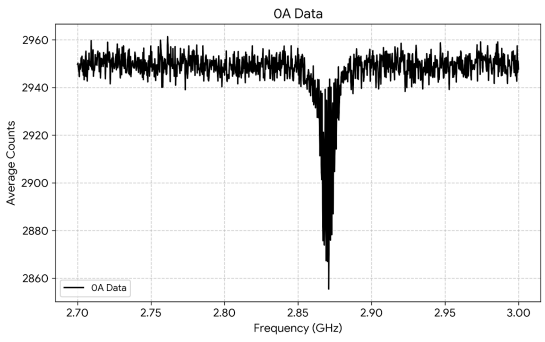

(a) CW-ODMR spectrum at zero magnetic field.

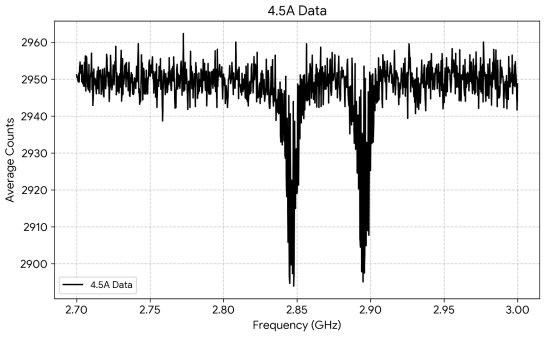

(b) CW-ODMR spectrum in the presence of an external magnetic field.

Figure 4.3: CW-ODMR spectra (a) At zero magnetic field showing a single resonance dip corresponding to zero-field splitting. (b) In the presence of an external magnetic field showing Zeeman splitting into two distinct resonance dips.

And fig 4.3b shows the ODMR spectrum at some uniform external magnetic field, which was applied by the pair of Helmholtz coils, two dips can be observed for the transitions $m_s = 0 \rightarrow m_s = -1$ and $m_s = 0 \rightarrow m_s = +1$, observed resonance frequency from this ODMR spectrum are 2.846 GHz and 2.897 GHz respectively.

Although CW-ODMR is the simplest way to implement, the ODMR spectrum obtained from it has many drawbacks, because the optical and microwave power boarding dips are broad and of low contrast. It can be observed in fig 4.3 that the signal-to-noise ratio is also bad in this mode of detection, so it becomes difficult to resolve the splitting of levels when an external magnetic field is present and also to measure the resonance frequencies with precision.

To overcome these issues and get more precise results with higher resolution, other techniques are employed.

4.3.2 Pulse Wave-odmr

Pulsed Mode ODMR is done using the technique described in the section 3.3.2. This technique is better than CW mode as it helps to reduce the effects of the optical and microwave power broadening. Fig 4.4 show the results of the PW-ODMR. As it can be observed, the FWHM and contrast are not optimal in the first measurement, so it various optimisations, including change of the laser and microwave power were done to get the optimal results.

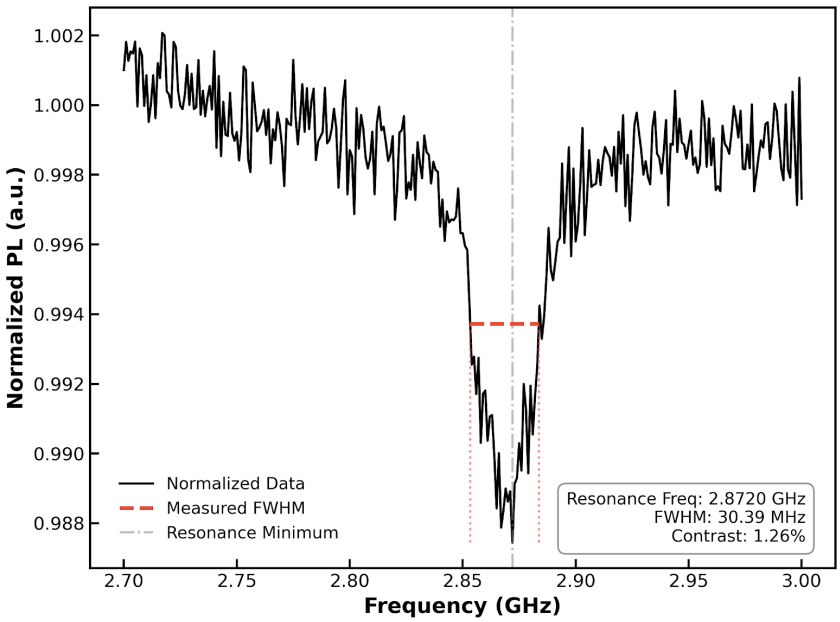

Figure 4.4: PW-ODMR spectrum before optimization, showing broad linewidth and low contrast.

Optimisation of ODMR signal

The ODMR spectrum is heavily dependent on the microwave and optical power being delivered to the system. It was observed that the optimal signal, corresponding to an optical power of 60 mW, was obtained.

For optimising the signal, corresponding to the microwave power, which was being delivered by the Mirny synthesiser, a digital attenuation was given to the microwave antenna ranging from 0.0dB to 30dB; this attenuation reduces the power delivered to the microwave antenna.

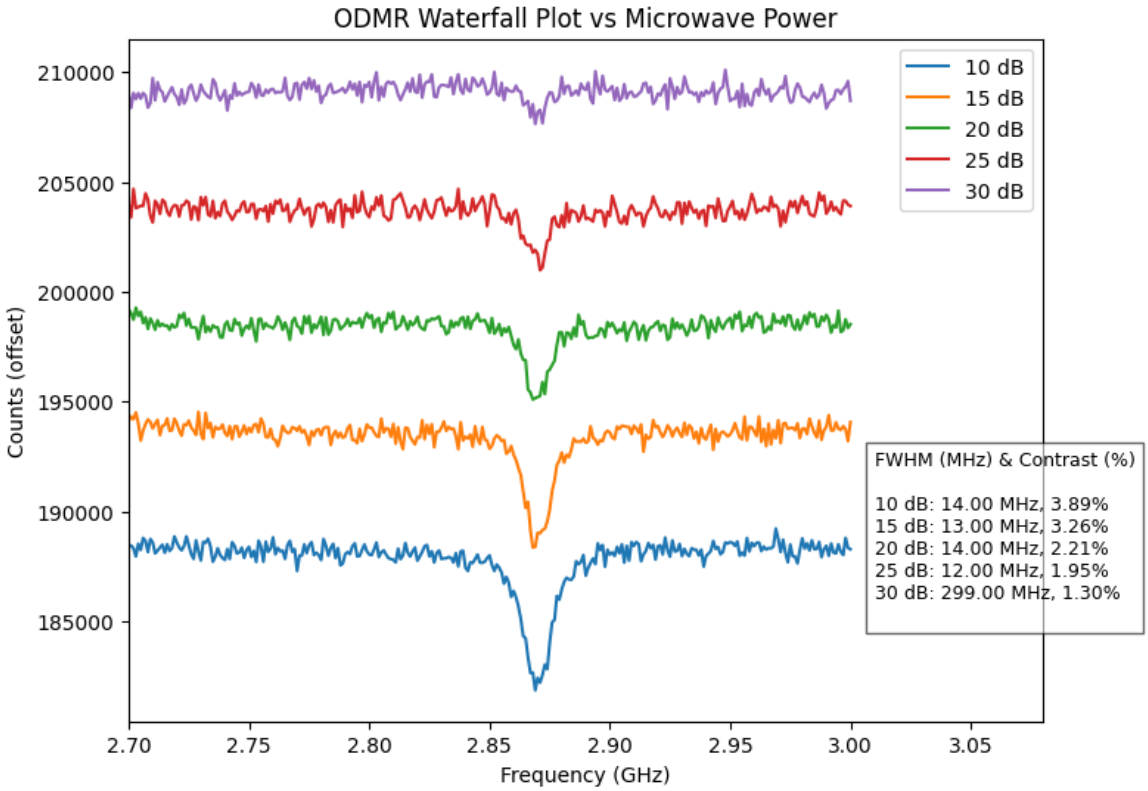

Figure 4.5: Variation of FWHM and contrast of the ODMR signal with microwave power (controlled via attenuation).

Fig 4.5 shows the variation of the FWHM and contrast with changing microwave power. It can be observed that, when the power of the applied microwave field is highest, the signal obtained has the highest contrast, but the linewidth is also high because of the power broadening.

As microwave power is reduced, the signal strength also decreases, and at the same time, the effect of the power broadening is also reduced, so there is always a trade-off between one and the other. So we choose an attenuation such that we can have the optimal signal. In this case, a 15dB attenuation is chosen.

Optimized signal

As we have the optimal parameter for the laser and microwave power, we can vary the other parameters like microwave pulse length, laser polarisation time and acquisition time period. Pulse sequence shown in fig 3.8 shows the optimised parameters that were used for acquiring the data.

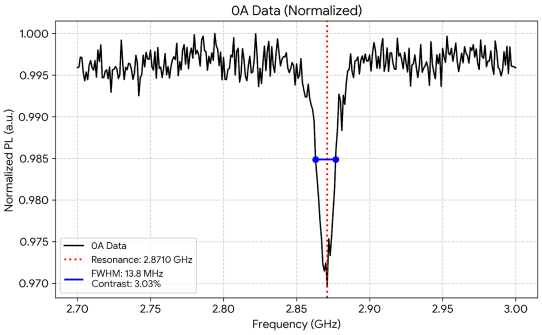

(a) PW-ODMR spectrum at zero magnetic field.

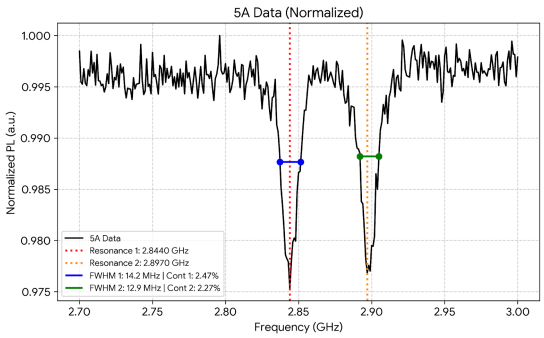

(b) PW-ODMR spectrum in the presence of an external magnetic field.

Figure 4.6: Pulsed ODMR spectra under optimized conditions. (a) At zero magnetic field showing a single resonance dip corresponding to zero-field splitting. (b) In the presence of an external magnetic field showing Zeeman splitting into two distinct resonance dips.

We can clearly resolve the resonance frequency in this mode, it can be seen in fig 4.6a when no external magnetic field is applied the resonance frequency for $m_s = 0 \rightarrow m_s = \pm 1$ transition is simply zero field splitting i.e. 2.8710 GHz.

For the application of a uniform magnetic field, a pair of Helmholtz coils was used. Fig 4.6b shows the ODMR spectrum recorded in the presence of an external magnetic field. It is clearly visible that the single resonance dip has been resolved into two resonance dips, which shows that the degeneracy between states $m_s = \pm 1$ has been lifted due to Zeeman effect. These two resonance dips correspond to the transition $m_s = 0 \rightarrow m_s = -1$ and $m_s = 0 \rightarrow m_s = +1$ with resonance frequency 2.8440 GHz and 2.8970 GHz respectively.

Having knowledge of the exact resonance frequency is vital for quantum computing and information. But it can be observed in the fig 4.6 that the dips are not that sharp; there is a lot of noise because of various factors. So to extract the exact resonance frequencies another method was employed.

4.3.3 Differential ODMR

Differential ODMR is an advanced measurement technique, which is discussed in section 3.3.3. This technique enhances the sensitivity and signal-to-noise ratio of conventional ODMR measurements. Since optimization of each parameter was already

done in the pulsed wave ODMR, no further optimization of the signal was needed. The parameters, as shown in fig 3.9, were used.

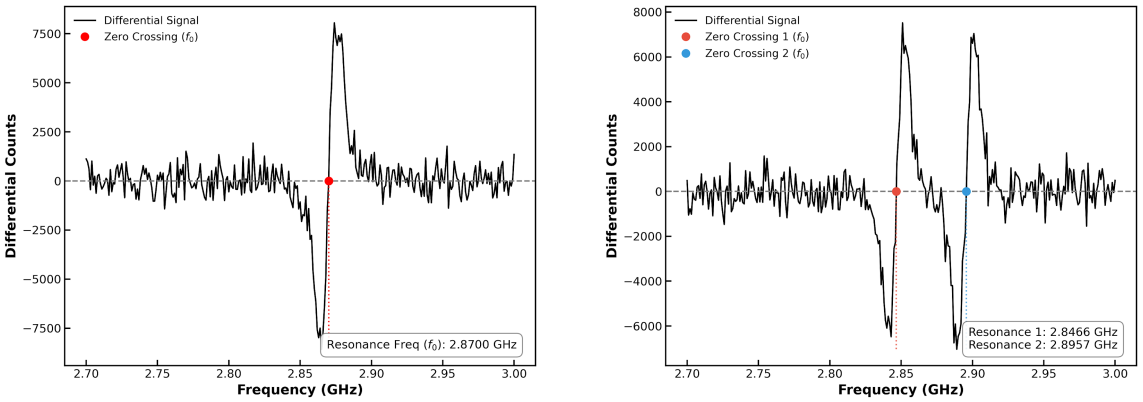

(a) Zero magnetic field

(b) With applied magnetic field

Figure 4.7: Differential ODMR continuous-wave measurements at (a) zero magnetic field and (b) when an external magnetic field is applied.

We can clearly see the difference in both the method. Here, the resonance frequency is described as a point at zero-crossing, as shown in fig 4.7. In the fig 4.7a, when no magnetic field is applied the resonance frequency is clearly resolved at exactly 2.870 GHz, which is zero-field splitting(i.e., transition between $m_s = 0 \rightarrow m_s s = \pm 1$).

Fig 4.7b shows the differential ODMR spectrum in the when magnetic field is applied , clearly resolves the splitting of the $m_s = \pm 1$ state. The resonance frequency for the transition of $m_s = 0 \rightarrow m_s = -1$ and $m_s = 0 \rightarrow m_s = +1$ can be easily found by the zero-crossing point. Resonance frequency for the transitions $m_s = 0 \rightarrow m_s = -1$ and $m_s = 0 \rightarrow m_s = +1$ are 2.8466 GHz and 2.8957 GHz respectively.

Compared to PW-ODMR, the differential ODMR provides much sharper and well-defined resonance frequency. Since this method depends on the zero-crossing point instead of the broad dip, so it significantly improves the precision in the frequency estimation.

Thus, the differential technique is a powerful method for resolving the transition frequency, it detects more accurately and detects the small shifts. This technique can also be used to track the varying magnetic field, as it is easier and faster to track the shifting resonance frequency.

4.4 Magnetic field sensing using confocal microscope

Magnetic field sensing using NV centres has been discussed in section 2.3.2, on the application of the external magnetic field, the degenerate states starts to show splitting

which is directly proportional to the applied magnetic field, because of zeeman effect, splitting is given as:

$$\Delta\nu = \nu_+ - \nu_- = 2\gamma_e \mathbf{B_0} \cdot \hat{\mathbf{u}}_\mathbf{i} \tag{4.1}$$

where $\gamma_e = 2.8\ MHz/G$ is the gyromagnetic ratio of the electron and $\hat{\boldsymbol{u}}_{\boldsymbol{i}}$ represents the i^{th} NV axis.

The dot product in Eq. (4.1) indicates that the NV centre is sensitive only to the component of the magnetic field along its quantization axis. Each NV centre has a well-defined crystallographic orientation inside the diamond lattice, represented by the unit vector $\hat{\boldsymbol{u}}_i$.

The effective magnetic field experienced by the NV spin is the projection of the applied magnetic field along the NV axis, not the total magnetic field applied. Let's say the angle between the applied magnetic field and NV axis θ, then the splitting is given as:

$$\Delta\nu = \nu_+ - \nu_- = 2\gamma_e B_0 \cos\theta \tag{4.2}$$

If the magnetic field is applied parallel to the quantisation axis i.e $\theta = 0$ then the slope of splitting is optimal and given as :

$$\frac{\Delta\nu}{B_0} = 2\gamma_e \approx 5.6 \text{ MHz/G}. \tag{4.3}$$

Magnetic field sensing using a confocal microscope is an efficient way for for detecting highly localised magnetic fields, such as those produced by single spins and nanoscale structures, by isolating individual NV centres with nanoscale spatial resolution. Single NV centres are therefore ideal for probing local magnetic fields at the nanoscale [27].

In contrast, this work utilises high-density (ensemble) NV centres, where isolating single NVs is not feasible. Ensemble-based measurements are better suited for detecting bulk and spatially averaged magnetic fields, as the collective fluorescence from many NV centers significantly enhances the signal-to-noise ratio. This leads to improved magnetic field sensitivity, typically in the nanoTesla to picoTesla per root Hertz (nT/$\sqrt{\text{Hz}}$ to pT/$\sqrt{\text{Hz}}$) range under optimized conditions. But in the confocal microscope, the signal is from a small volume of diamond, which leads to reduced signal as compared to open set up and sensitivity is given as :

$$\eta \propto \frac{\Delta\nu}{C\sqrt{R}} \tag{4.4}$$

where $\Delta\nu$ is the linewidth (FWHM) of the ODMR resonance, C is the ODMR contrast, and R is the count rate per second. So with reduced R, the sensitivity.

4.4.1 Magnetic field callibration

For applying the external magnetic field, an electromagnet in a Helmholtz configuration was used. This configuration provides a nearly uniform magnetic field in the region between the coils, where the diamond sample is mounted.

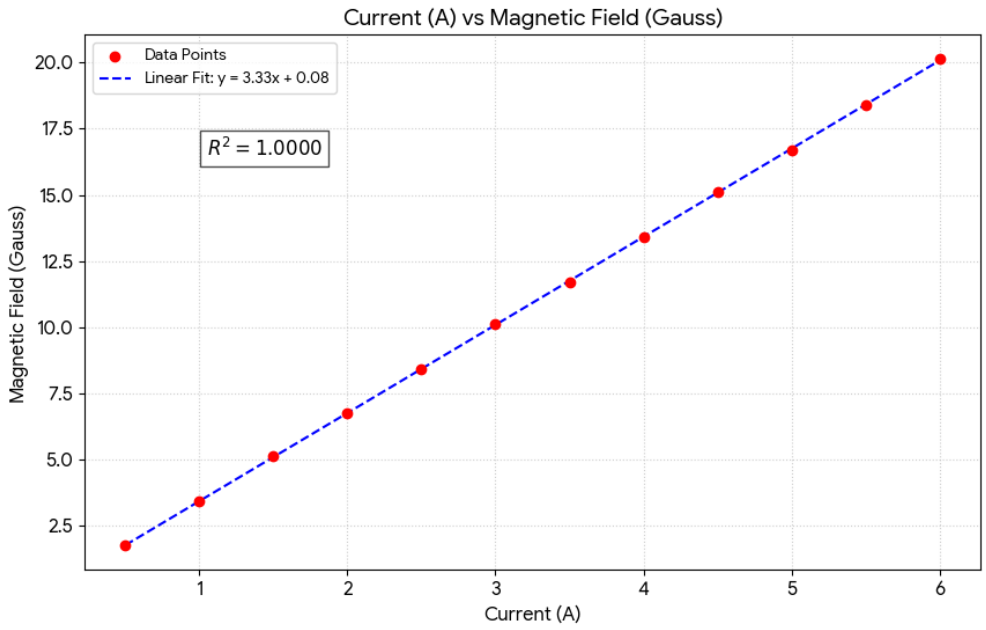

Figure 4.8: Calibration curve showing the variation of magnetic field with applied current for the Helmholtz coil configuration.

To control the strength of the magnetic field, a variable current was supplied to the coils. The current was varied in steps of 0.5 A. The relationship between the applied current and the resulting magnetic field was recorded at the place where the diamond is mounted using a gaussmeter, as shown in Fig. 4.8.

4.4.2 Pulse Mode method

In pulse mode, the data was recorded by sweeping from 2.70 GHz to 3.0 GHz in step of $1MHz$, by varying the current in coils in steps of 0.5 A from 0 to 5.5A. Fig 4.9 shows the ODMR spectrum in the form of a waterfall plot at different external magnetic fields. Lorentzian curves are fitted to calculate the resonance frequencies, full width at half maximum (FWHM), and contrast of each ODMR dip, results of which are summarised within the figure only.

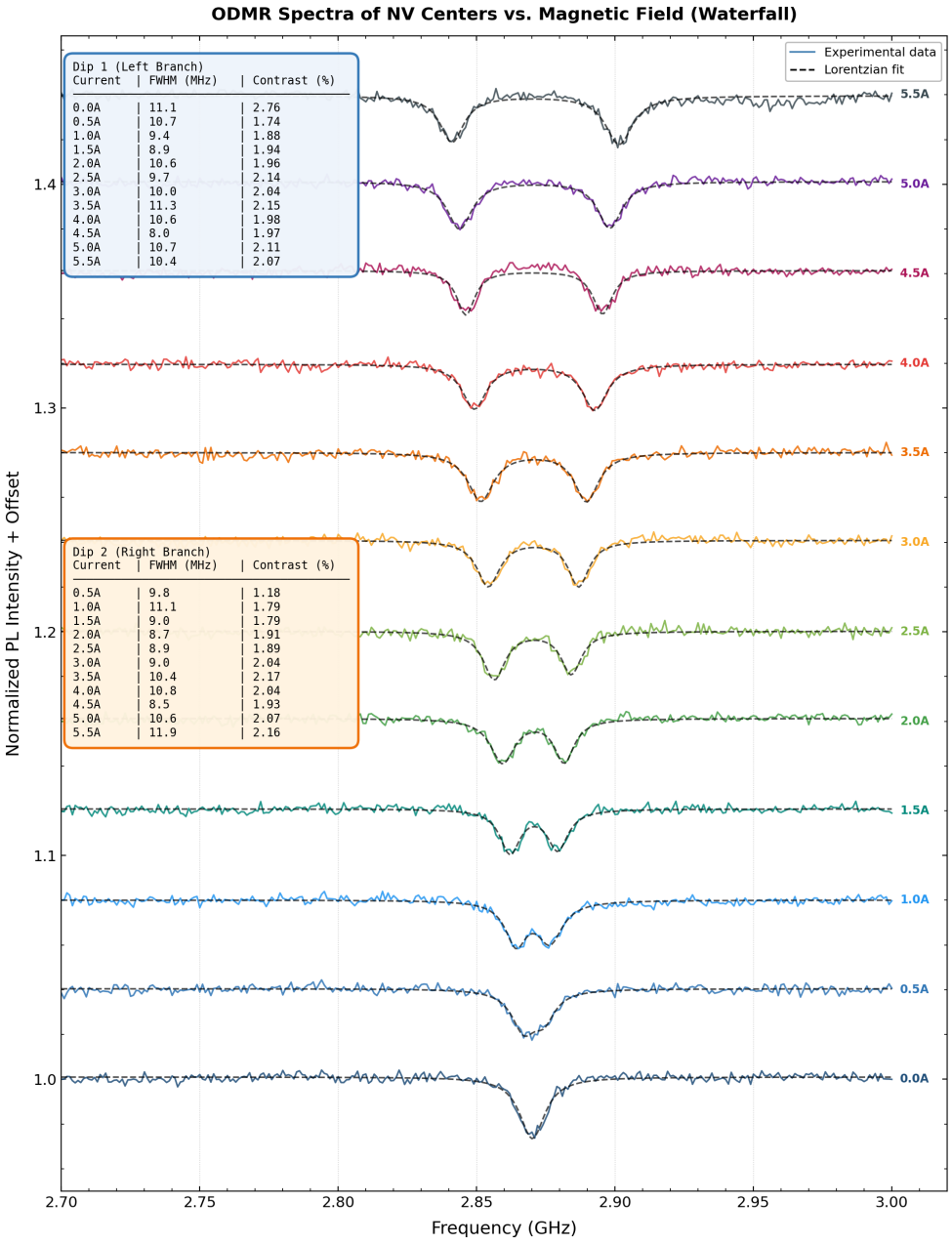

Figure 4.9: Waterfall plot of pulsed ODMR spectra of NV centres for different applied magnetic fields. Dashed lines represent Lorentzian fits used to extract the resonance frequency, linewidth (FWHM), and contrast. Insets show the extracted FWHM and contrast values for both left and right branches.

To evaluate the orientation of the NV axis with respect to the applied magnetic field, magnetic field vs Zeeman splitting was plotted as shown in fig 4.10. A linear fit yielded a slope of 3.186 MHz. Now using eq. 4.2 and eq. 4.3 we get the angle between the NV axis and applied magnetic field θ is given as :

$$\cos\theta = \frac{3.186}{5.6} \approx 0.569 \;\Rightarrow\; \theta \approx 55^\circ \tag{4.5}$$

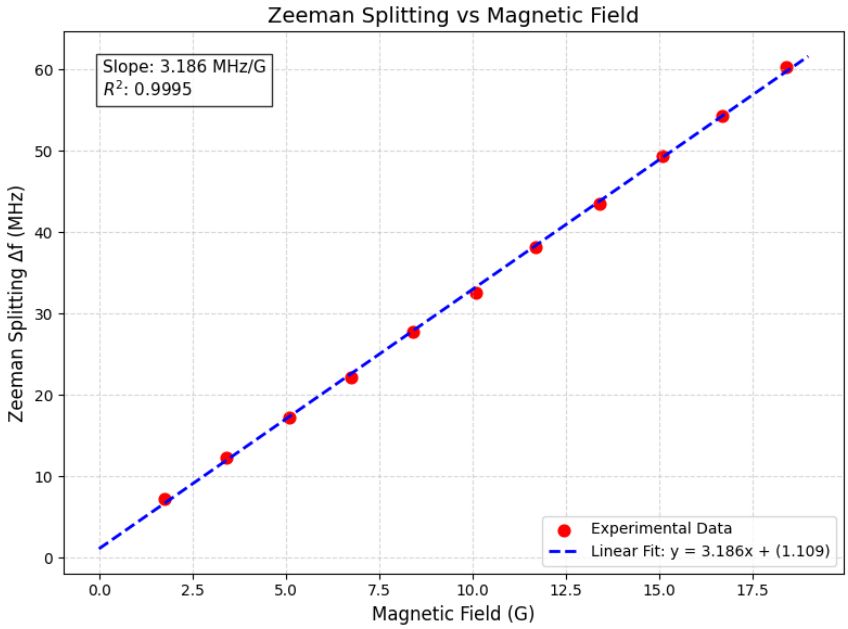

Figure 4.10: Zeeman splitting (Δf) as a function of the applied magnetic field. The slope of 3.186 MHz/G confirms the linear Zeeman effect and is used to determine the angle between the NV axis and applied magnetic field.

Sensitivity analysis

The sensitivity of magnetic field is calculated using :

$$\eta_{\mathrm{PW}} \approx P_f \frac{\Delta\nu_{\mathrm{PW}}}{C_{\mathrm{PW}}\sqrt{R}} \cdot \frac{1}{\gamma_e} \tag{4.6}$$

where $P_f = 0.77$ is the Lorentzian lineshape factor [28, 29], $\gamma_e = 2.8 MHz/G$, other values taken from the ODMR spectrum corresponding to 4A, the calculated sensitivity for parameters

$$\nu_0 = 2.8925\ \mathrm{GHz}, \quad \Delta\nu_{\mathrm{PW}} = 10.860\ \mathrm{MHz}, \quad C_{\mathrm{PW}} = 1.935\%, \quad R = 5.24 \times 10^7\ \mathrm{s}^{-1} \tag{4.7}$$

$$\eta_{\mathrm{PW}} = 0.7698 \times \frac{1}{2.8 \times 10^6\ \mathrm{Hz/G}} \times \frac{10.860 \times 10^6\ \mathrm{Hz}}{0.01935 \times \sqrt{5.24 \times 10^7}} \tag{4.8}$$

$$\boxed{\eta_{\mathrm{PW}} \approx 2.13\,\mu\mathrm{T}/\sqrt{\mathrm{Hz}}}. \tag{4.9}$$

The current sensitivity is mainly constrained by the linewidth ($\Delta\nu_{\mathrm{PW}} = 10.860$ MHz) and relatively low contrast ($C_{\mathrm{PW}} = 1.935\%$). Even though pulsed ODMR enables a better manipulation of spin dynamics than the cw counterpart, the sensitivity stays at the $\mu\mathrm{T}/\sqrt{\mathrm{Hz}}$ level owing to several factors, including power broadening, microwave

instability, and inefficiency of optical collection.

Enhancing sensitivity can be done by improving the pulse sequence and minimising other limiting factors, such as decoherence and inefficient optical collection; this could bring the sensitivity to the nT/$\sqrt{\text{Hz}}$ level.

4.4.3 Differential Method

In differential mode, the data was again recorded by sweeping from 2.70 GHz to 3.0 GHz in steps of 1 MHz and $\Delta f = 10\ MHz$, by varying the current in coils in steps of 0.5 A from 0 to 5.5A. Fig 4.11 shows the ODMR spectrum in the form of a waterfall plot at different external magnetic fields.

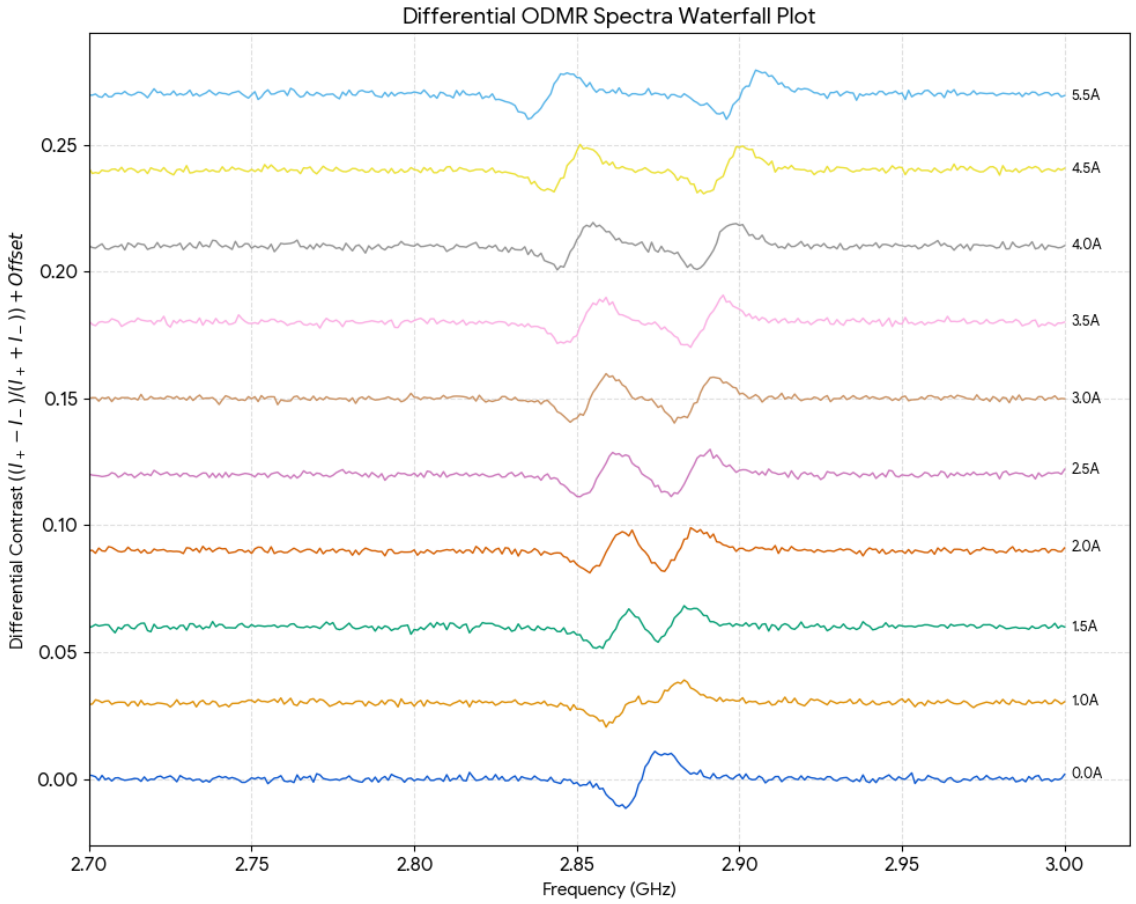

Figure 4.11: Waterfall plot of differential ODMR spectra of NV centres under varying external magnetic fields. The differential technique enhances the slope of the resonance signal, improving sensitivity to small frequency shifts.

To evaluate the orientation of the NV axis with respect to the applied magnetic field, magnetic field vs Zeeman splitting was plotted as shown in fig 4.12. A linear fit yielded a slope of 3.292 $MHz/Gauss$. Now using eq. 4.2 and eq. 4.3 we get the

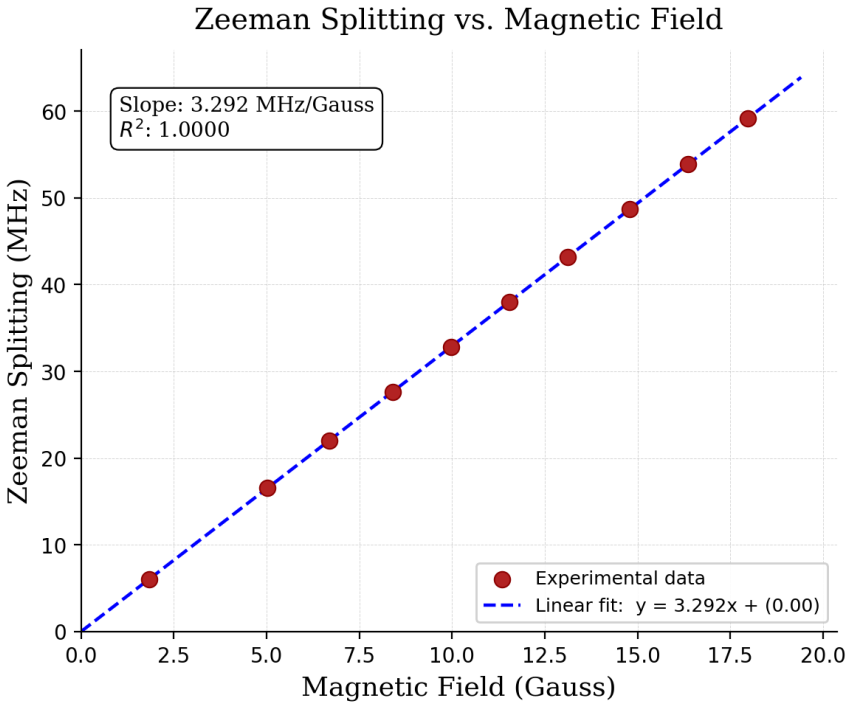

Figure 4.12: Zeeman splitting (Δf) as a function of the applied magnetic field for differential ODMR. The slope of 3.292 MHz/G confirms the linear Zeeman response and is used to extract the NV axis orientation.

angle between the NV axis and applied magnetic field θ :

$$\cos\theta = \frac{3.292}{5.6} \approx 0.587 \;\Rightarrow\; \theta \approx 53.9^\circ \tag{4.10}$$

Comparing it with θ obtained in eq: 4.5, shows a deviation of only 1°, which can be because of experimental uncertainties such as the curve fitting in PW mode for Lorentzian peaks, frequency resolution and noise in both the modes.

Sensitivity Analysis

In the differential measurement mode, the magnetic field sensitivity is calculated using the slope method. The differential signal is defined as:

$$S(f) = I\left(f + \frac{\Delta f}{2}\right) - I\left(f - \frac{\Delta f}{2}\right) \tag{4.11}$$

which approximates the first derivative of the ODMR lineshape, with the steepest slope at the zero-crossing point corresponding to the spin resonance frequency f_0.

The magnetic field sensitivity is given by [28, 29]:

$$\eta = \frac{\sigma_S}{\frac{dS}{df} \cdot \gamma_e \cdot \sqrt{T_{\text{meas}}}} \tag{4.12}$$

where σ_S is the standard deviation of the differential signal, dS/df is the slope at the zero-crossing point, $\gamma_e = 28.024\ \mathrm{GHz\,T^{-1}}$ is the NV electron gyromagnetic ratio, and Tmeas is the total photon acquisition time per frequency point, which was 6ms.Other parameters are extracted from data corresponding to 4.5A as:

$$\frac{dS}{df} \approx 2.399 \times 10^{-3}\ \mathrm{counts\,Hz^{-1}} \tag{4.13}$$

$$\sigma_S \approx 563\ \mathrm{counts} \tag{4.14}$$

Substituting into Eq. (A.11):

$$\eta = \frac{563}{2.39 \times 10^{-3} \times 28.024 \times 10^{9} \times \sqrt{6.00 \times 10^{-3}}} \tag{4.15}$$

$$\boxed{\eta \approx 77.2\ \mu\mathrm{T}/\sqrt{\mathrm{Hz}}} \tag{4.16}$$

However, the sensitivity obtained for differential ODMR is noticeably less as compared to that of pulsed ODMR ($\sim 2.13\,\mu\mathrm{T}/\sqrt{\mathrm{Hz}}$). Even though the differential method provides an improved slope around the resonant frequency, the sensitivity still strongly depends on the signal-to-noise ratio. In the present case, the differential noise outweighs the slope enhancement, resulting in reduced overall sensitivity.

Further optimisation can be done by improving the photon collection efficiency, frequency modulation and the background noise. This method can be helpful in calculating the varying magnetic field if optimised better.

Chapter 5

Conclusion and Future Work

5.1 Conclusion

The primary goal of this thesis was to develop a confocal microscope with the full control system in order to study NV centers in diamond samples for different applications. The following experiments have been performed with the constructed instrument:

- Scanning has been performed to reveal the density of NV centers in the sample. The high density of NV centers in the sample did not allow to find the individual NV center.
- ODMR spectrum measurements were performed to illustrate the zero-field splitting effect both in the ground state and excited state.
- Different pulses sequences were used to explore the effect of Zeeman splitting and to identify the resonant frequencies.
- It is demonstrated that a differential ODMR is the best technique to improve the accuracy of measurement of resonant frequencies due to noise reduction and increased signal contrast.
- In addition, it has been shown that NV centers can be used as a magnetic field sensor.

5.2 Future Outlook

Since confocal microscope with full control system is ready. Future work will focus on isotopically engineered diamond samples, which could involve the following:

- Measuring low-doped diamond samples in order to isolate and address single NV centers.
- Coherent manipulation of spins via, for example, Rabi oscillation experiments and characterization of spin coherence parameters such as T_2 and T_1 relaxation times of the spins.
- Exploiting isotopically purified diamond samples to implement more sophisticated quantum logic, such as quantum gates, as described in Section 2.6.2.

Bibliography

[1] V. M. Acosta, *Optical Magnetometry with Nitrogen-Vacancy Centers in Diamond*, Doctor of philosophy dissertation, University of California, Berkeley, Berkeley, CA (2011).

[2] V. Kavata, *Quantum Sensing with NV Centers in Diamond*, Doctor rerum naturalium (dr. rer. nat.), Georg-August-Universität Göttingen, Göttingen, Germany (2023), doctoral Programme PROPHYS, Georg-August University School of Science (GAUSS).

[3] M. W. Doherty, N. B. Manson, P. Delaney, F. Jelezko, J. Wrachtrup, and L. C. Hollenberg, Physics Reports **528**, 1 (2013).

[4] P. Neumann, *Towards a room temperature solid state quantum processor — The nitrogen-vacancy center in diamond*, Ph.D. thesis, University of Stuttgart (2012).

[5] A. V. S., *Optically Detected Magnetic Resonance of Nitrogen Vacancy Centers in Diamond*, Ph.D. thesis, Indian Institute of Science Education and Research (IISER) Pune (2019).

[6] J. H. Shim, I. Niemeyer, J. Zhang, and D. Suter, Europhysics Letters (EPL) **99**, 40004 (2012).

[7] B. Smeltzer, J. McIntyre, and L. Childress, Physical Review A **80**, 050302 (2009).

[8] M. A. Nielsen and I. L. Chuang, *Quantum Computation and Quantum Information* (Cambridge University Press, 2000).

[9] A. Montanaro, npj Quantum Information **2**, 15023 (2016).

[10] P. Wittek, *Quantum Machine Learning* (Academic Press, 2014).

[11] J. I. Cirac and P. Zoller, Physical Review Letters **74**, 4091 (1995).

[12] M. Saffman, T. G. Walker, and K. Mølmer, Reviews of Modern Physics **82**, 2313 (2010).

[13] F. Jelezko and J. Wrachtrup, physica status solidi (a) **203**, 3207 (2006).

[14] J. Wrachtrup and F. Jelezko, Journal of Physics: Condensed Matter **18**, S807 (2006).

[15] A. Gruber, A. Dräbenstedt, C. Tietz, L. Fleury, J. Wrachtrup, and C. von Borczyskowski, Science **276**, 2012 (1997).

[16] R. J. Narayan, R. D. Boehm, and A. V. Sumant, Materials Today **15**, 434 (2012).

[17] J. E. Graebner, in *Diamond: Electronic Properties and Applications*, edited by L. S. Pan and D. R. Kania (Springer US, Boston, MA, 1995) pp. 285–318.

[18] F. P. Bundy, H. T. Hall, H. M. Strong, and R. H. Wentorf, Nature **176**, 51 (1955).

[19] S. Pezzagna, D. Rogalla, D. Wildanger, J. Meijer, and A. Zaitsev, Physica Status Solidi (a) **207**, 2194 (2010).

[20] D. M. Toyli, C. D. Weis, G. D. Fuchs, T. Schenkel, and D. D. Awschalom, Nano Letters **10**, 3168 (2010).

[21] P. Balasubramanian, *Towards Quantum Technologies with Color Centers in Diamond*, Ph.D. thesis, Universität Ulm (2020), phD Dissertation.

[22] M. V. G. Dutt, L. Childress, L. Jiang, E. Togan, J. Maze, F. Jelezko, A. S. Zibrov, P. R. Hemmer, and M. D. Lukin, Science **316**, 1312 (2007).

[23] M. Steiner, Towards diamond-based quantum computers (2009).

[24] Y. Li *et al.*, Micromachines **14**, 1823 (2023).

[25] K. Ambal *et al.*, arXiv preprint arXiv:1808.05580 (2018).

[26] P. Parashar *et al.*, Scientific Reports **12**, 12609 (2022).

[27] J. R. Maze, P. L. Stanwix, J. S. Hodges, S. Hong, J. M. Taylor, P. Cappellaro, L. Jiang, M. V. G. Dutt, E. Togan, A. S. Zibrov, A. Yacoby, R. L. Walsworth, and M. D. Lukin, Nature **455**, 644 (2008).

[28] L. Rondin, J.-P. Tetienne, T. Hingant, J.-F. Roch, P. Maletinsky, and V. Jacques, Reports on Progress in Physics **77**, 056503 (2014).

[29] J. F. Barry, J. M. Schloss, E. Bauch, M. J. Turner, C. A. Hart, L. M. Pham, and R. L. Walsworth, Reviews of Modern Physics **92**, 015004 (2020).

Appendix A

Additional Derivations / Data

A.0.1 Derivation of the Sensitivity Formula

The derivation of the sensitivity formula for the differential ODMR magnetometer begins with the Lorentzian ODMR lineshape and its shot-noise limit.

Step 1: ODMR Lineshape

The fluorescence intensity as a function of microwave frequency f follows a Lorentzian dip:

$$I(f) = S_0 \left[1 - C \cdot \frac{(\Delta\nu/2)^2}{(f - f_0)^2 + (\Delta\nu/2)^2}\right] \tag{A.1}$$

where S_0 is the off-resonance baseline photon count rate, C is the ODMR contrast, f_0 is the resonance frequency, and $\Delta\nu$ is the full width at half maximum (FWHM).

Step 2: Differential Signal

In the differential method, two photon count rates are recorded at frequencies symmetrically detuned about f by a modulation depth ε:

$$I_\pm = I\left(f \pm \frac{\varepsilon}{2}\right) \tag{A.2}$$

The differential signal is:

$$\Delta I = I_+ - I_- \tag{A.3}$$

Applying a first-order Taylor expansion of $I(f)$ about f and substituting into Eq. (A.3):

$$\Delta I = \left[I(f) + \frac{\varepsilon}{2}\frac{dI}{df} + \frac{1}{2}\left(\frac{\varepsilon}{2}\right)^2 \frac{d^2I}{df^2} \right] - \left[I(f) - \frac{\varepsilon}{2}\frac{dI}{df} + \frac{1}{2}\left(\frac{\varepsilon}{2}\right)^2 \frac{d^2I}{df^2} \right] \tag{A.4}$$

All even-order terms cancel exactly, yielding:

$$\Delta I \approx \varepsilon \cdot \frac{dI}{df}, \qquad \varepsilon \ll \Delta\nu \tag{A.5}$$

The differential signal is therefore directly proportional to the local slope of the Lorentzian lineshape. The derivative of Eq. (A.1) is:

$$\frac{dI}{df} = -S_0 C \cdot \frac{(\Delta\nu/2)^2 \cdot 2(f - f_0)}{\left[(f - f_0)^2 + (\Delta\nu/2)^2\right]^2} \tag{A.6}$$

This is an antisymmetric function of $(f - f_0)$, producing the dispersive S-shaped error signal observed experimentally. Importantly, $dI/df = 0$ at $f = f_0$, so the differential signal has a zero crossing precisely at the spin resonance frequency.

Step 3: Shot Noise Floor

The fundamental noise limit in photon counting is shot noise. For a mean photon count rate N_p measured over a total acquisition time T_{meas}, the shot noise standard deviation is:

$$\sigma_S = \sqrt{N_p \cdot T_{\text{meas}}} \tag{A.7}$$

To normalise to a 1 Hz measurement bandwidth, σ_S is divided by $\sqrt{T_{\text{meas}}}$, giving the noise spectral density:

$$\tilde{\sigma}_S = \frac{\sigma_S}{\sqrt{T_{\text{meas}}}} \tag{A.8}$$

Step 4: Minimum Detectable Frequency Shift

The minimum detectable frequency shift $\delta f_{\min}$ is reached when the signal change equals the noise spectral density:

$$\delta f_{\min} = \frac{\tilde{\sigma}_S}{\left|\frac{dS}{df}\right|} = \frac{\sigma_S}{\frac{dS}{df} \cdot \sqrt{T_{\text{meas}}}} \tag{A.9}$$

where dS/df is evaluated at the zero-crossing point $f = f_0$, where the slope is steepest.

Step 5: Conversion to Magnetic Field

From the linear Zeeman relation for9 NV symmetry axis:

$$\delta f = \gamma_e \, \delta B \tag{A.10}$$

where $\gamma_e = 28.024 \text{ GHz T}^{-1}$ is the NV electron gyromagnetic ratio. When an external magnetic field δB is applied, the resonance shifts from f_0 to $f_0 + \gamma_e \, \delta B$, displacing the zero crossing of ΔI by the same amount. The minimum detectable magnetic field is therefore:

$$\boxed{\eta = \frac{\delta f_{\min}}{\gamma_e} = \frac{\sigma_S}{\dfrac{dS}{df} \cdot \gamma_e \cdot \sqrt{T_{\text{meas}}}}} \tag{A.11}$$

eq A.11 give the sensitivity of detection of magnetic field in differential ODMR.